Applied Ocean Research 120 (2022) 103057

Contents lists available at ScienceDirect

Applied Ocean Research

journal homepage: www.elsevier.com/locate/apor

Time domain simulation of marine riser vortex-induced vibrations in three-dimensional currents

Sang Woo Kim [a,*], Svein Sævik [a], Jie Wu [b], Bernt Johan Leira [a]

[a] Department of Marine Technology, Norwegian University of Science and Technology, 7491, Trondheim, Norway
[b] SINTEF Ocean, 7052 Trondheim, Norway

ARTICLE INFO

Keywords:
Vortex-induced vibration
Time domain VIV model
3D current
Marine riser
Fatigue damage

ABSTRACT

One of the major uncertainties related to present Vortex-Induced Vibrations (VIV) prediction practice is related to the simplification of real multi-directional current profiles into equivalent uni-directional ones. This study addresses the correlation between a recently updated time domain model and data from VIV experiments including both two- and three-dimensional (2D and 3D) currents. The test riser and current profile were modeled in three different ways, including 2D & 3D current profiles and linear & nonlinear models, as a basis for discussing the results from various perspectives. As a first step, VIV simulations with a nonlinear riser model including actual current profiles were carried out, demonstrating a good correlation with test data for 2D current and low velocity 3D current. However, simulated VIV displacements were somewhat underestimated for the high velocity 3D current profiles. With reference to literature noting possible drag reduction for 3D current cases, drag coefficient sensitivity studies were carried out, demonstrating better correlation for 3D current cases at high velocities. Then, the VIV fatigue damages obtained by the three alternative structural and current modeling procedures were compared to each other in a case study. The locations of the maximum fatigue damages differed between methods, and it was demonstrated that prediction using uni-directional current does not always lead to the highest fatigue damage. In conclusion, it was demonstrated that the time domain VIV model can describe the 3D current VIV, and by doing that, it was found that present VIV prediction practice can be improved.

1. Introduction

Vortex-Induced Vibrations (VIV) is a resonant vibration phenomena caused by the interaction between fluid and structure which is governed by a number of variables (Williamson and Govardhan, 2008; Gabbai and Benaroya, 2005; Sarpkaya, 2004; Blevins, 1977). As the mechanism of VIV is complex, it is challenging to capture the related response phenomena by numerical methods. VIV is very important for the design of marine risers that are exposed to currents and waves during operation (DNV.GL, 2017). VIV induces bending stress in the riser that can lead to fatigue and as a result also drag amplification due to the increased projection area in the flow direction (Jhingran, 2008). Drag amplification increases the static displacement and tension of the riser system. For high mode vibrations, there might also be significant axial vibration components that can contribute to instability and additional fatigue damage in the riser system.

Many model tests were carried out to investigate VIV responses of marine risers under uni-directional flow conditions, e.g., (Huse, 1997; Braaten and Lie, 2005; Vandiver et al., 2006, 2009). In these tests, the direction of the incoming flow does not vary along the extension of the riser. IL VIV response frequency was normally twice the CF frequency and non-stationary VIV responses (frequency, displacement, tension, etc.) were observed with increasing response mode orders even under constant flow conditions (Swithenbank, 2007; Wu et al., 2016). Marine risers may also be subjected to a three-dimensional flow field as ocean current directions frequently vary across the water column. The structure itself can also be three-dimensional in space. This means that the local normal speed direction will vary along the extension of the riser. Hence, the local direction of cross-flow and in-line may vary along the riser. The cross-flow force at a specific cross-section may interact with the in-line force at other locations. The influences of three-dimensional flow on VIV responses have been subjected to limited studies. One of the reasons is that it is difficult to create three-dimensional flows in laboratory conditions. There is also a lack of prediction tools which can include 3D flow effects. Therefore, the directional variation of the current has so far been neglected in riser design practice. Design current

* Corresponding author.
E-mail address: sangwoo.kim@ntnu.no (S.W. Kim).

https://doi.org/10.1016/j.apor.2022.103057
Received 21 September 2021; Received in revised form 2 December 2021; Accepted 7 January 2022
Available online 1 February 2022

Nomenclature

α	Angle between arms (Horizontal plane)
Δf_x	In-line synchronization range
Δf_y	Cross-flow synchronization range
$\dot{x}_{\text{rel}}$	Relative structure velocities in local x direction
$\dot{y}_{\text{rel}}$	Relative structure velocities in local y direction
$\hat{f}_{0,x}$	Non-dimensional frequency of maximum energy transfer of in-line
$\hat{f}_{0,y}$	Non-dimensional frequency of maximum energy transfer of cross-flow
ω	Frequency of VIV
$\phi_{\dot{x}_{\text{rel}}}$	Phase of cylinder in-line velocity
$\phi_{\dot{y}_{\text{rel}}}$	Phase of cylinder cross-flow velocity
$\phi_{\text{exc,x}}$	Phase of the in-line vortex shedding force
$\phi_{\text{exc,y}}$	Phase of the cross-flow vortex shedding force
ρ	Fluid density
τ	Angle between riser and bottom (Vertical plane)
ζ	Structural damping ratio
c	Velocity of sound in the material of the riser
C_D	Drag coefficient
C_M	Inertia coefficient
$C_{v,x}$	In-line vortex shedding force coefficient
$C_{v,y}$	Cross-flow vortex shedding force coefficient
D_c	Directionality
D_e	Outer diameter
D_i	Inner diameter
$D_{fat,i}$	Fatigue damage of the i^{th} cross-section.
EA	Axial stiffness
EI	Bending stiffness
F_D	Drag force
F_I	Inertia force
f_{v}	Shedding frequency
F_{FK}	Froude-Kriloff force
F_{M_a}	Added mass force
$F_{v,x}$	In-line vortex shedding force
$F_{v,y}$	Cross-flow vortex shedding force
k	Wavenumber of vibration
L	Riser length
m	Mass per unit length
Re	Reynolds number
S_c	Sheardeness
St	Strouhal number
T	Tension
U	Current velocity
$V_{c,CF}$	Critical flow speeds associated with axial vibration frequency caused by cross-flow
$V_{c,IL}$	Critical flow speeds associated with axial vibration frequency caused by in-line
x_0	Amplitude of VIV
x_c	Principal axis in relation to Directionality
$x_{L'}$	Local in-line direction at each cross-section
x_L	Local x-direction of the accelerometer
y_c	Normal axis in relation to Directionality
$y_{L'}$	Local cross-flow direction at each cross-section
y_L	Local y-direction of the accelerometer
z	vertical coordinate from riser top to bottom
$\phi_{\text{exc},x}$	Instantaneous phases of the vortex shedding forces of in-line
$\phi_{\text{exc},y}$	Instantaneous phases of the vortex shedding forces of cross-flow
σ_z	Bending stress
θ_x	Phase difference between the cylinder cross-flow velocity and the cross-flow vortex shedding force
θ_y	Phase difference between the cylinder cross-flow velocity and the cross-flow vortex shedding force
$M_x(t)$	Bending moments induced by the cross-flow
$M_y(t)$	Bending moments induced by the in-line
u_{n,x_c}	Velocity components in principal direction
u_{n,y_c}	Velocity components in normal direction
$\mathbf{r}_n$	Structure local response
$\mathbf{u}_n$	Incoming flow component (normal to riser)
$\mathbf{v}_n$	Relative flow velocity ($= \mathbf{u}_n - \dot{\mathbf{r}}_n$)
2D	Two dimensional
3D	Three dimensional
CF	Cross-flow
CFD	Computational fluid dynamics
FEM	Finite element method
Geo	Geometry
IL	In-line
LU	Linear structural model and Uni-directional currents
NDP	Norwegian Deepwater Programme
NLM	Non-linear structural model and Multi-directional currents
NM	Linear structural model and Multi-directional currents
PSD	Power spectral density
SCR	Steel catenary riser
STD	Standard deviations
VIV	Vortex-induced vibrations
WAFO	Wave Analysis for Fatigue and Oceanography

profiles are normally simplified to be uni-directional (Voie et al., 2016), which introduces significant uncertainties in riser design.

Semi-empirical models formulated in the frequency domain are widely used for riser VIV design analyses. Representative software is VIVANA (Larsen et al., 2017), Shear7 (Vandiver and Li, 2005), and VIVA (Triantafyllou et al., 1999). The software based on frequency domain methods relies on hydrodynamic force coefficients generalized from VIV model test data, which are formulated as functions of non-dimensional frequency and amplitude ratio. The frequency domain method has normally been limited to predicting VIV responses under 2D constant flow conditions in the present design practice. Prediction of VIV responses under 3D flow conditions is still under academic investigations (Schiller et al., 2014). Even if the current profile is not 3D, similar problems occur when the riser configuration itself is 3D. Moreover, structural non-linearity (e.g. pipe–soil interactions, tension variations) cannot be handled by frequency domain methods.

To overcome the limits of the frequency domain methods, time domain analysis is needed. Computational fluid dynamics (CFD) based on the Navier–Stokes equation is a well known time domain method. By solving the governing equation around the riser, the vortex shedding processes can be predicted precisely. There have been attempts to apply the CFD method for analysis of the marine riser VIV (Huang et al., 2007; Kamble and Chen, 2016; Wang et al., 2017). However, the VIV design of marine risers requires a large number of VIV simulations for various sea states. Even for one CFD simulation, extensive computing resources are needed. Therefore, it is difficult to apply CFD in real riser design.

As an alternative, semi-empirical time domain models have been developed. The wake oscillator model is one of the alternative methods which is based on solving the Van der Pol equation. Since it was proposed for the first time by Hartlen and Currie (1970), different wake oscillators have been developed to describe coupled CF and IL motion of rigid cylinders in uniform flow (Facchinetti et al., 2004; Ogink and Metrikine, 2010; Srinil and Zanganeh, 2012). Further studies have been made with respect to flexible cylinder tests in uniform or linearly sheared currents (Violette et al., 2007; Kang and Jia, 2013; Gao et al., 2021). A major challenge of wake oscillators is to find correlations between some empirical parameters and their physical meaning, which makes it difficult to generalize to other conditions because of these constraints. In addition, so far, no attempts have been made with respect to analyzing VIV response under 3D current conditions by application of wake oscillator models.

A semi-empirical time domain VIV model based on the synchronization concept was proposed by Thorsen et al. (2014, 2016, 2017). The model has been improved to describe CF and IL coupled motions (Ulveseter et al., 2019; Kim et al., 2021a) and has been validated with respect to various deepwater riser model tests in 2D uniform and shear flow (Ulveseter et al., 2018, 2019; Kim et al., 2021a,b). Also, the empirical coefficient set of the model has been optimized to fit with the test results. However, the model has not yet been applied for VIV analysis in 3D currents.

Experimental results for 3D current conditions for model validation are sparse. To explore the VIV responses in 3D currents, rotating rig experiments were conducted in the MARINTEK ocean basin (Mo, 1999). The tests aimed to investigate VIV response in various 2D and 3D flow conditions. A test was also performed to study the influence of a directional flow on the VIV response of a steel catenary riser (SCR) model (Lie, 2001). However, the numerical studies carried out on the basis of these data have so far transformed the 3D currents into 2D profiles (Moe et al., 2004; Riemer-Sørensen et al., 2019). It is therefore necessary to further study these test data in order to obtain more insights on VIV responses in 3D flow conditions.

The main objective of the present study is to evaluate the performance of the time domain VIV model which is described in Kim et al. (2021a) under 3D current conditions by comparing the predictions with the rotating rig test results (Mo, 1999). This is followed by a numerical case study to evaluate the impact on the present design practice based on using 2D and 3D current in the riser VIV analysis. Section 2 gives detailed descriptions of the rotating rig test and current profiles. In order to validate the test results or compare fatigue analysis results from various perspectives, three types of numerical riser models are described in Section 3. The theoretical background of the time domain VIV model and its hydrodynamic coefficients are described in Section 4. In Section 5, validations of the time domain VIV model with the nonlinear riser model are discussed in terms of top tension, frequency, and displacement. In Section 6, the results in terms of fatigue damage according to the three riser modeling methods are discussed and compared. This is followed by a drag coefficient sensitivity study for the 3D current VIV cases included in Section 7. The main findings and conclusions of the study are summarized in Section 8.

2. Model test of the 3D current VIV

2.1. Set-ups of the rotating rig test

The main purpose of the test was to investigate the VIV of a long riser subjected to two- and three-dimensional currents (2D and 3D current). The test rig consisted of a vertical cylinder, arms, and pretension arrangement (spring, hinge, and beam), see Fig. 1. The upper arms and lower arm were attached to both ends of the cylinder, and the upper arms have different lengths to each other. The riser was connected between the upper and lower arm through the pretension arrangement. The bi-directional accelerometers were installed on the riser at 10 different positions, however, Accelerometer 3 and Accelerometer 10 were failed. By means of the universal joints at the ends of the riser, all translations and torsional degrees of freedom were kept fixed while the bending rotations were free. The top of the riser could freely move in a vertical direction in connection to the pretension arrangement. The test rig was rotated three or four cycles about the rotating axis for each case. The set-up of the test rig for 2D current profiles is illustrated in Fig. 1.

Three-dimensional current profiles could be obtained by rotating the pretension arrangement and upper arm together while the lower arm was fixed. The sheared level of the current profiles could be controlled by changing the length of the upper arm and the location of the movable hinge along the fixed beam. The number of riser configurations considered in the test was seven, and two configurations were excluded in the present study. This was because the angle between the upper and lower arms was too large (165 °) for two cases (Geometry 5 and Geometry 6), which was judged to be unrealistic compared to real current profiles. Detailed configurations for each case are illustrated in Fig. 2, and each geometry is hereafter abbreviated as Geo. The detailed information of each test set-up is also summarized in Table 1.

2.2. Details of current profiles

As illustrated in Fig. 2, each riser had a different angle of inclination to the bottom plane (x–y plane). In order to figure out the effective current profile that the riser felt during rotation, it was necessary to estimate the current velocity along the length of the riser. The current velocity, u_n which is perpendicular to the riser axis is the main source of the VIV response at each cross-section. u_n can be estimated by geometrical analysis, and the distributions of u_n for each Geometry are illustrated in Fig. 3a. u_n was non-dimensionalized by the maximum value of $u_{n,max}$ along the riser, and vertical coordinate from riser top to bottom, z was non-dimensionalized by the riser length. It should be noted that the $u_{n,max}$ differed between geometries due to different angles, τ at the same rotational speed of the test rig, see Fig. 2. $u_{n,max}$ for each geometry can be estimated as $U sin(\tau)$.

To characterize each current profile in more detail, two non-dimensional parameters were introduced. The Sheardeness, S_c is defined as the distribution of the current velocity along the length of the riser, and the Directionality, D_c represents the distribution of current velocity relative to the main direction. The main direction of current was defined as half of the angle between the upper and lower arms, α, and named as the principal axis, x_c. The axis which is normal to the principal direction was defined as the normal axis, y_c. Sheardeness and Directionality can be expressed in Eqs. (1) and (2).

$$D_c = \frac{rms(u_{n,y_c})}{rms(u_{n,x_c})} = \sqrt{\frac{\sum_{i=1}^{n} u_{n,y_c,i}^2}{\sum_{i=1}^{n} u_{n,x_c,i}^2}} \tag{1}$$

$$S_c = \frac{\sigma_{u_{n,x_c}}}{\bar{u}_{n,x_c,i}} = \frac{\sqrt{\frac{1}{n}\sum_{i=1}^{n}\left(u_{n,x_c,i} - \bar{u}_{n,x_c,i}\right)^2}}{\frac{1}{n}\sum_{i=1}^{n} u_{n,x_c,i}} \tag{2}$$

where, u_{n,x_c} and u_{n,y_c} are the velocity components in principal- and normal direction at a specific point of the riser.

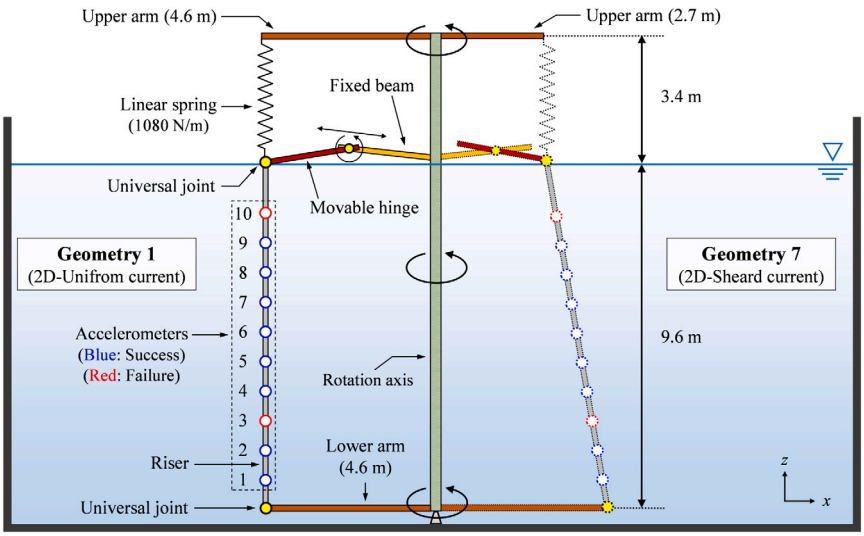

Fig. 1. Examples of test set-ups for 2D current profiles (Geometry 1 and Geometry 7).

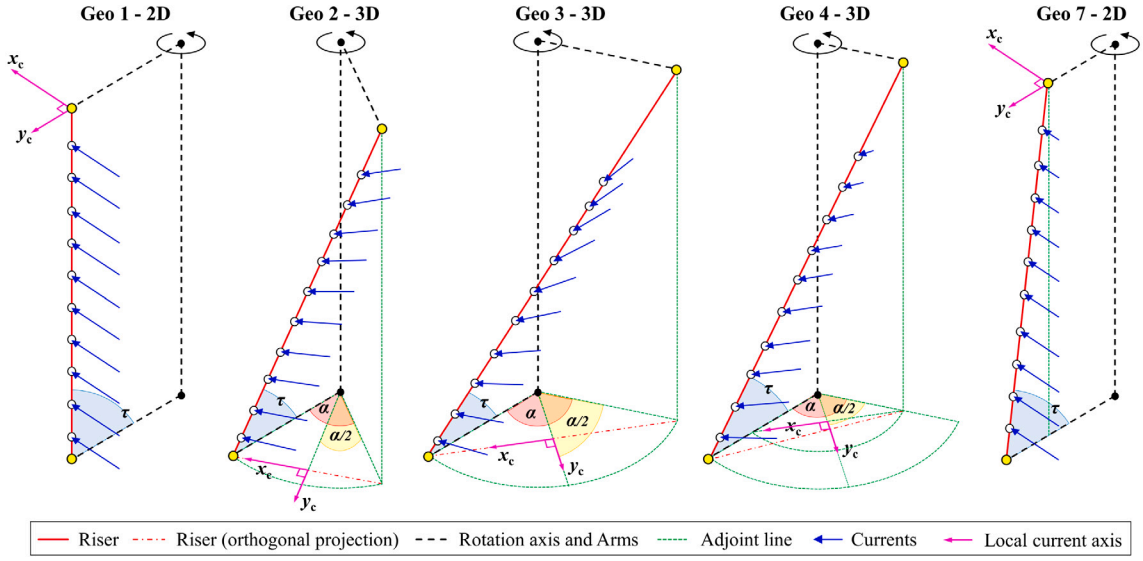

Fig. 2. Detailed configuration of each Geometry.

Table 1
Key data for the rotating rig riser model.

Geometry No.	1	2	3	4	7
Mass per unit length [kg/m], m			0.543		
Outer diameter [m], D_e			0.023		
Inner diameter [m], D_i			0.015		
Bending stiffness [N m^2], EI			14.6		
Axial stiffness [N], EA			3.1 $\times 10^5$		
Riser length [m], L	9.60	11.10	12.60	12.03	10.10
Pretensions [N], T	701	703	709	688	700
Radius of upper arm [m]	4.6	4.6	4.6	2.7	2.7
Radius of lower arm [m]	4.6	4.6	4.6	4.6	4.6
Angle b/w arms (Horizontal plane) [°], α	0.5	59.6	119.6	116.2	3.6
Angle b/w riser and bottom (Vertical plane) [°], τ	89.4	65.5	50.7	58.3	79.0

By means of both parameters, it was possible to interpret the 3D current profiles in 2D planes when u_n can be decomposed in the directions of x_c and y_c. The decomposed current velocities in principal- and normal direction are plotted in Fig. 3b. The upper row figures illustrates the currents distributions in x_c–y_c plane (Directionality), and the lower ones represents the current distribution in the x_c–z plane. The velocities and the z coordinates were non-dimensionalized by the maximum current velocity, $u_{n,max}$, and riser length, L, respectively. The detailed current information are summarized in Table 2.

As summarized in Fig. 3b and Table 2, Shearedness of Geo 1, Geo 2, and Geo 3 were almost zero. The difference between these geometries, was the angle between the arms, α resulting in variation of Directionality. Also, the current profiles were symmetric about the center of the riser in the length direction. Meanwhile, the current profiles of Geo

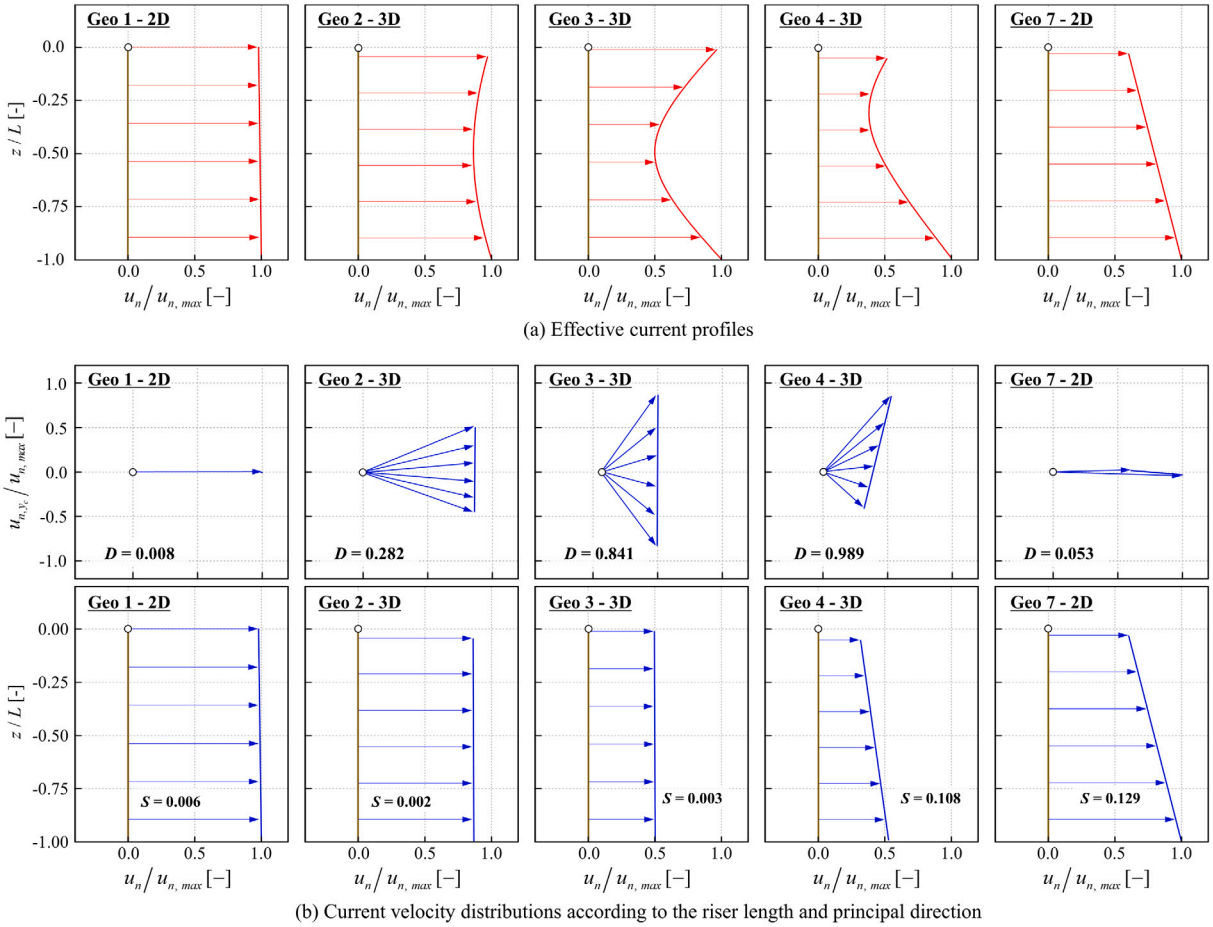

Fig. 3. Non-dimensionalized current velocity function of the riser length and principal direction of the current (z/L = 0.0 — Top of the riser, z/L = −1.0 — Bottom of the riser).

Table 2
Key data for current profiles of each Geometry.

Geometry No.	1	2	3	4	7
Rotation velocity [m/s], U			0.3–1.8		
Current type [–]	2D current	3D current	3D current	3D current	2D current
Sheardness [–]	0.006	0.002	0.003	0.108	0.129
Directionality [–]	0.008	0.282	0.841	0.989	0.053

4 and Geo 7 showed high Shearednesss due to the short upper arm. So, the current profiles were asymmetric about the center of the riser in the length direction. Especially, for Geo 4, Directionality was also higher than in other cases. This implies that the current profile for Geo 3 and Geo 4 would induce the chaotic VIV responses. The Sheardness, Directionality, and current profiles type will be used to discuss VIV response results in relation to the 3D level of current profiles.

3. Numerical simulations of the rotating rig test

3.1. Numerical modeling of the test riser

The test riser was numerically modeled in RIFLEX (SINTEF Ocean, 2017), which is based on the 3D finite element method (FEM). Three different modeling methods are introduced to shed light on the VIV responses in 3D currents.

The first riser model, see Fig. 4a, is a non-linear structural model that can describe both the non-linear boundary conditions and current profiles of the test. The rotation of the test rig was simulated by the prescribed motion. The rotations were introduced at the end of the lower and upper arms, and at the end of the fixed beam connected to the movable hinge. The movable hinge and linear spring of the pretensioning system were modeled using bar elements. The movable hinge has a triangle connection to prevent the translation motion (i.e., out of plane motion). For Geo 4 and Geo 7, the length of the upper arm and fixed beam differs from Geo 1, Geo 2, and Geo 3. The non-linear structural model is referred to as Model-NLM (Non-Linear structural model with Multi-directional currents). Two linearized riser models were introduced where the inclined risers were changed into vertical risers. To apply the same top tension level as the test, the measured mean tension during the rotation was applied for each case. To derive corresponding current profiles for vertical riser, incoming flow vectors which are normal to the riser axis and their attack of angles were calculated. When reconstructing current profiles, two methods were considered. The former is based on a multi-directional current profile considering a variation of attack angle of incoming flows at each cross-section, the latter is based on a uni-directional current profile having the same attack of angle for all current components along the riser length. The modeling methods are referred to as Model-LM (Linear structural model with Multi-directional currents) and Model-LU (Linear structural model with Uni-directional currents), respectively. Model-LM and Model-LU are illustrated in Fig. 4b and c. The Model-LU represents the traditional modeling method with reference to the frequency domain method.

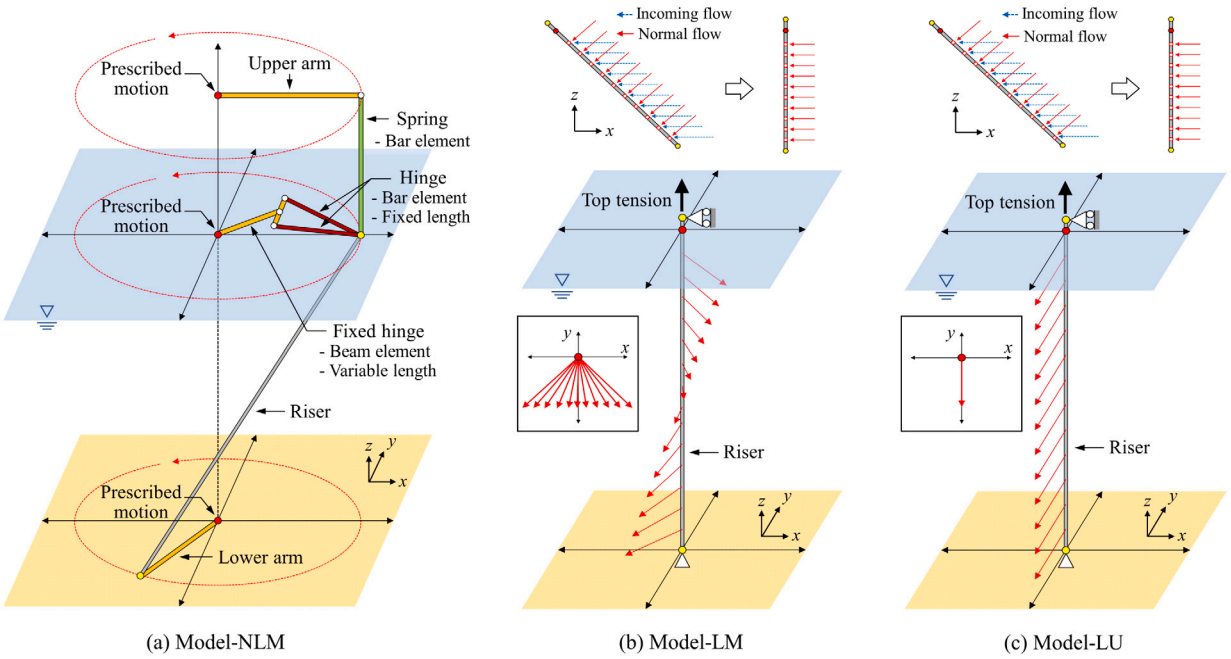

(a) Model-NLM (b) Model-LM (c) Model-LU

Fig. 4. Illustration of numerical riser models (NLM: Non-linear structural model + Multi-directional currents, LM: Linear structural model + Multi-directional currents, LU: Linear structural model + Uni-directional currents).

Table 3
Numerical input parameters and filtering ranges.

Parameters	Value
Strouhal number, St	0.17
Number of elements	500
Number of time steps per CF period	60
Structural damping ratio, ζ	0.7%
Filtering bandwidths (Acceleration)	$f_v/3$ Hz–$2f_v$ Hz
Filtering bandwidths (Tension)	$f_v/3$ Hz–$4f_v$ Hz

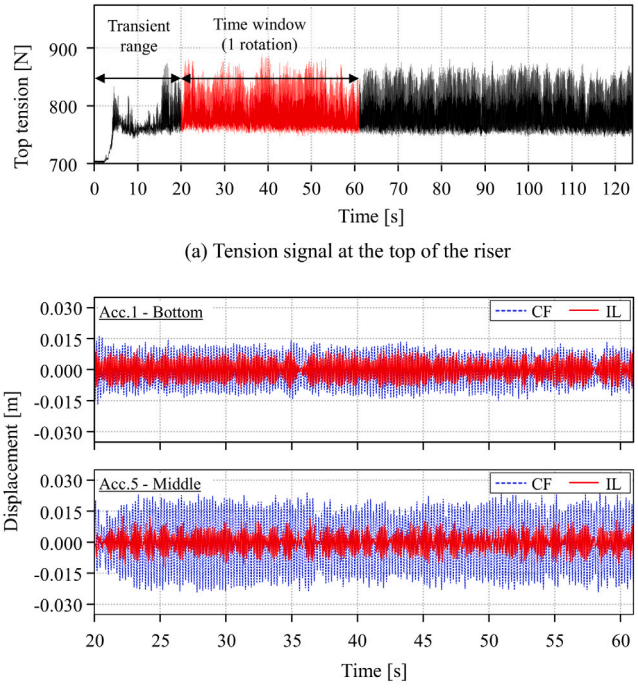

(a) Tension signal at the top of the riser

(b) Displacement signals near bottom and mid point of the riser

Fig. 5. Raw signals for top tension and displacements (Geometry 1, $U = 0.71$ m/s).

3.2. Signal post-processing and numerical set-up

Disturbance of the fluid in the test tank might have developed as the number of cycles was getting higher. To minimize the error due to the fluid disturbance, raw signals of the test were extracted from a range between the first- and second rotation excluding an initial transient range. The total length of the extracted signal corresponds to one rotation, containing roughly 200 to 250 cross-flow cycles. In addition, bandpass filtering based on the shedding frequency, f_v ($= StU_{max}/D_e$) was applied for the measured signals. The upper- and lower cutoff frequency for the measured accelerations was set to be $f_v/3$ and $2f_v$ to remove noises. For tension signals, the bandwidth value was doubled ($4f_v$) to investigate the VIV-induced axial oscillations. An example of post-processed signals for the test is shown in Fig. 5. The same length of the time window and range of filtering was applied to simulation results. Modeling details are summarized in Table 3.

3.3. Transformation of the coordinate system

The measured signals in the test followed the orientation of the accelerometers at each cross-section. However, the local coordinate system, x_L and y_L axis of the accelerometers did not always coincide with in-line or cross-flow at each cross-section. This was because the static configuration of the riser varied according to the current profile type. The static configuration was determined by the main flow direction, and the directions of the local currents were varied along the riser. Another reason was the material properties of the test riser. The test riser was specially manufactured by rubber. Therefore, the torsional stiffness of the riser was lower than for a steel riser. For that reason, even for 2D uniform flow, some of the sensors attached to the rubber were twisted and not perfectly aligned with the other sensors.

In order to compare the test results and simulations quantitatively, a united coordinate system for the two sets of results was introduced. For the tests cases, the in-line and cross-flow at each cross-section were transformed into the VIV coordinate system, $x_{L'}$ and $y_{L'}$ regardless of the x_L and y_L. The $x_{L'}$ is in-line, and the $y_{L'}$ is the cross-flow. Therefore, the definitions of the $x_{L'}$ and $y_{L'}$ were different for every

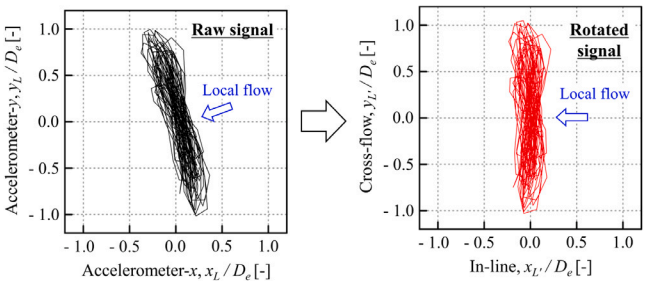

Fig. 6. Example of the coordinate system transformation.

cross-section. The same approach was applied to the simulations. An example of a coordinate system transformation between the local and VIV coordinate system is illustrated in Fig. 6.

4. Time domain VIV model

4.1. Hydrodynamic load formulation

The hydrodynamic load model associated with VIV was proposed by combining the vortex shedding force terms with Morison's equation by Thorsen et al. (2017). Therefore, the load model is based on the strip theory and only considers an incoming flow component, $\mathbf{u}_n$ that is normal to the cylinder axis as shown in Fig. 7a. Each force term of the load model is defined in the direction of the incoming flow velocity, $\mathbf{u}_n$, the structure local response, $\mathbf{r}_n$, and the relative flow velocity, $\mathbf{v}_n$ (= $\mathbf{u}_n - \dot{\mathbf{r}}_n$). Relevant vectors and local coordinate system in a cross-section of the cylinder are defined in Fig. 7b, and the hydrodynamic forces on the cylinder (per unit length) are represented by Eq. (3) by Ulveseter et al. (2018):

$$\mathbf{F}_n = \underbrace{\underbrace{\underbrace{C_M \rho \frac{\pi D_e^2}{4} \dot{\mathbf{u}}_n}_{\text{Froude-Kriloff force } (\mathbf{F}_{FK})} - \underbrace{(C_M - 1)\rho \frac{\pi D_e^2}{4} \ddot{\mathbf{r}}_n}_{\text{Added mass force } (\mathbf{F}_{M_a})}}_{\text{Inertia force } (\mathbf{F}_I)} + \underbrace{\frac{1}{2}\rho D_e C_D |\mathbf{v}_n| \mathbf{v}_n}_{\text{Drag force } (\mathbf{F}_D)}}$$
$$+ \underbrace{\underbrace{\frac{1}{2}\rho D_e C_{v,x} |\mathbf{v}_n| \mathbf{v}_n \cos\phi_{\text{exc},x}}_{\text{IL vortex shedding force } (\mathbf{F}_{v,x})} + \underbrace{\frac{1}{2}\rho D_e C_{v,y} |\mathbf{v}_n| (\mathbf{j}_3 \times \mathbf{v}_n) \cos\phi_{\text{exc},y}}_{\text{CF vortex shedding force } (\mathbf{F}_{v,y})}}_{\text{Vortex shedding force}} \tag{3}$$

where, C_M, C_D, D_e, and ρ are the inertia coefficient, drag coefficient, cylinder diameter, and fluid density, respectively. $C_{v,x}$ and $C_{v,y}$ are in-line and cross-flow vortex shedding force coefficients; $\phi_{\text{exc},x}$ and $\phi_{\text{exc},y}$ are the in-line and cross-flow instantaneous phases of the vortex shedding forces.

The first three forces terms are inertia force, F_I (= $F_{FK} + F_{M_a}$) and drag force, F_D, while $F_{v,x}$ and $F_{v,y}$ are in-line and cross-flow vortex shedding forces. The cross-flow vortex shedding force represents a lift force in the local y direction which is a normal direction to the relative flow vector, $\mathbf{v}_n$, while the in-line vortex shedding force $F_{v,y}$ describes a fluctuating drag force in a local x direction which is in the same direction as $\mathbf{v}_n$. The definition of the vortex shedding forces vectors is based on the fact that the vortex shedding forces are in phase with respect to the relative structure velocity. The relative structure velocities in each local x and y direction are as follow:

$$\dot{y}_{\text{rel}} = \dot{\mathbf{r}}_n \cdot \frac{\mathbf{j}_3 \times \mathbf{v}_n}{|\mathbf{v}_n|} \tag{4}$$

$$\dot{x}_{\text{rel}} = \dot{\mathbf{r}}_n \cdot \frac{\mathbf{v}_n}{|\mathbf{v}_n|} \tag{5}$$

4.2. Synchronization of vortex shedding forces

Synchronization for VIV is a concept which describes the phase-coupling between force and response to obtain lock-in. $\phi_{\text{exc},x}$ and $\phi_{\text{exc},y}$ in Eq. (3) are used to control lock-in process. In order to realize the lock-in, the instantaneous frequency of vortex shedding force can be changed to match up with the instantaneous frequency of the relative velocity of the structure. The concept of cross-flow synchronization is illustrated in Fig. 8.

As illustrated in Fig. 8a, when the phase angle of the cross-flow vortex shedding force lags behind the phase angle of the relative structure velocity in y direction, let the instantaneous frequency of vortex shedding force increase to minimize the phase difference. In the opposite case, the instantaneous frequency of cross-flow vortex shedding force is decreased. Synchronizations are only permitted in the synchronization range which is determined based on experimental data as shown in Fig. 8b. The relationship between instantaneous frequency and phase angle, and the terms which are related to the synchronization of cross-flow are as follow:

$$\frac{d\phi_{\text{exc},y}}{dt} = 2\pi f_{\text{exc},y} = \frac{2\pi |\mathbf{v}_n|}{D} \hat{f}_{\text{exc},y} \tag{6}$$

$$\hat{f}_{\text{exc},y} = \hat{f}_{0,y} + \Delta\hat{f}_y \sin\theta_y \tag{7}$$

where, Δf_y, and $\hat{f}_{0,y}$ determine the cross-flow synchronization range and the non-dimensional frequency of maximum energy transfer. θ_y is the phase difference between the cylinder cross-flow velocity, $\phi_{\dot{y}_{\text{rel}}}$ and the cross-flow vortex shedding force, $\phi_{\text{exc},y}$, ($\theta_y = \phi_{\dot{y}_{\text{rel}}} - \phi_{\text{exc},y}$). $\phi_{\dot{y}_{\text{rel}}}$ can be numerically approximated at each time step (Thorsen et al., 2017).

In the cases of the in-line responses, there are a pure in-line response and an in-line response which is combined cross-flow motion. In this study, the combined in-line and cross-flow motion is the main consideration, and the frequency of in-line is approximately twice that of cross-flow in this case (Dahl et al., 2010). In order to describe this feature, the synchronization range of in-line response is set to be twice that of cross-flow while adapting the same synchronization principles as the cross-flow (Kim et al., 2021a). The terms for in-line synchronization can be formulated as follows:

$$\frac{d\phi_{\text{exc},x}}{dt} = 2\pi f_{\text{exc},x} = \frac{2\pi |\mathbf{v}_n|}{D} \hat{f}_{\text{exc},x} \tag{8}$$

$$\hat{f}_{\text{exc},x} = \hat{f}_{0,x} + \Delta\hat{f}_x \sin\theta_x \tag{9}$$

where, Δf_x, and $\hat{f}_{0,x}$ determine the cross-flow synchronization range and the non-dimensional frequency of maximum energy transfer. θ_x is the phase difference between the cylinder cross-flow velocity, $\phi_{\dot{x}_{\text{rel}}}$ and the cross-flow vortex shedding force, $\phi_{\text{exc},x}$ ($\theta_x = \phi_{\dot{x}_{\text{rel}}} - \phi_{\text{exc},x}$.)

The orthogonal motions in each local direction are independent of each other at the cylinder cross-section based on the synchronization. Synchronization also makes it possible to reflect key features of VIV. During the synchronization, the energy transfer from the fluid to the structure becomes positive resulting in increasing VIV amplitude and drag force. When the amplitude reaches a certain level, the energy transfer between damping and excitation will be balanced so that the amplitude can no longer increase. This is well known as a self-limiting process of VIV. Also, the out of phase components of each vortex shedding force contribute to the acceleration of structure, so the changes in the added mass force according to the VIV responses can be explained. In addition, as the VIV response develops, the effective diameter of the riser also increases. As a result, the deformation and drag force increase in the in-flow direction due to the drag amplification.

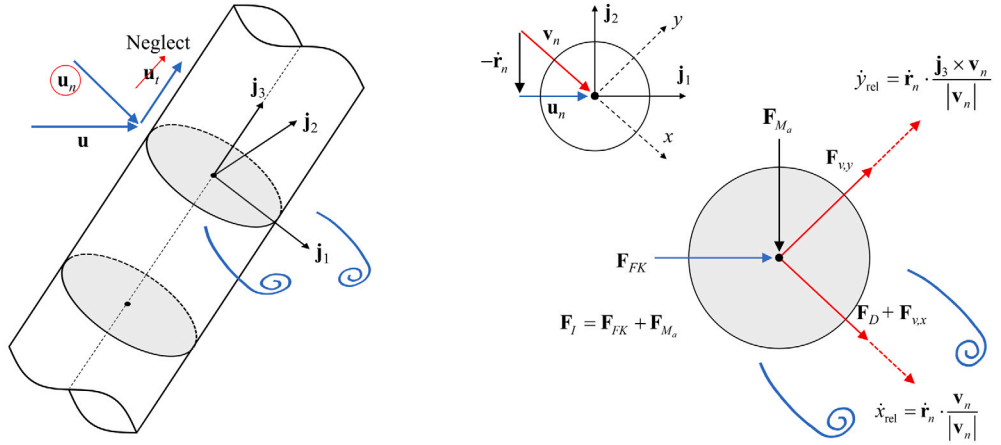

(a) 3D cylinder strip with an incoming flow (b) Hydrodynamic force terms at the cross-section

Fig. 7. A cylinder strip with the relevant vectors and local coordinate system.

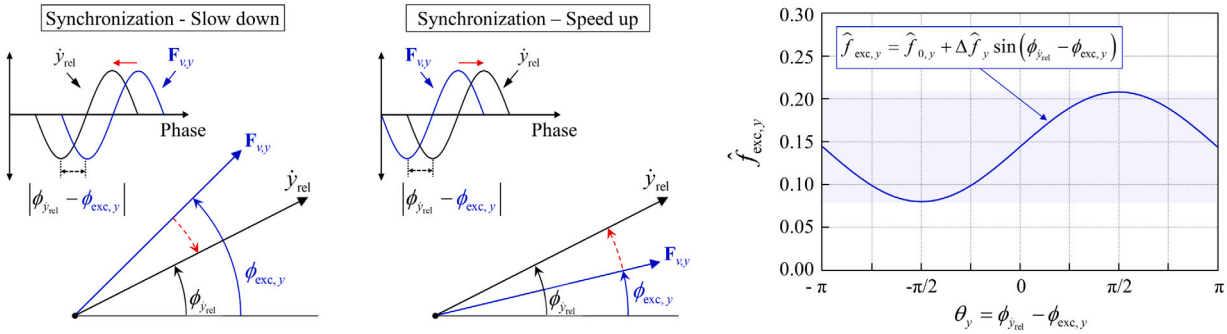

(a) The phase angle relationship between $\mathbf{F}_{v,y}$ and $\dot{y}_{\text{rel}}$ (b) Synchronization function of the cross-flow

Fig. 8. Illustration of the cross-flow synchronization.

4.3. Hydrodynamic coefficients

The time domain VIV model assumes that the empirical coefficients for hydrodynamic load and synchronization are constant regardless of non-dimensional variables. Since the empirical parameters were optimized and validated with the same hydrodynamic coefficient data used for VIVANA (Thorsen et al., 2017). The empirical parameter set has also been kept updated through validations with various marine riser tests after the initial optimization study. Therefore, in order to apply the optimized results to another VIV analysis, it is necessary to check the detailed conditions such as system stiffness, type of current profile, and Reynolds number.

For cross-flow and in-line combined response, the best-fit empirical hydrodynamic parameters were based on the Norwegian Deepwater Programme (NDP) high mode VIV test in uniform current conditions (Ulveseter et al., 2018). The stiffness of the NDP test riser was tension dominated, and Reynolds number (Re = 8.1 $\times 10^3$– 6.48 $\times$ 10^4) belongs to sub-critical ranges. Although the initial parameter set was slightly underestimated for the same riser in sheared currents (Drengsrud, 2019), the same empirical parameter set was validated for Hanøytangen test riser (Kim et al., 2021b,a). The high mode Hanøytangen tests were bending stiffness dominated with higher Reynolds numbers (Re = 1.2 $\times$ 10^4 - 5.88 $\times 10^5$). In the case of Rotating rig test risers, the stiffness of the riser is tension-dominated case, and the Reynolds number range (Re = 6.92 $\times$ 10^3–4.23 $\times 10^4$) is similar to the NDP high mode VIV test. So, the empirical parameter set for the NDP high mode VIV test was selected to investigate the correlation between tests and simulations. In the cases of the synchronization parameters, the parameters were according to Kim et al. (2021a). The details of the coefficients are described in Table 4.

Table 4
Empirical parameters of the time domain VIV models.

Parameters	C_D	C_M	$C_{v,y}$	$C_{v,x}$	$\hat{f}_{0,y}$	$\Delta\hat{f}_y$	$\hat{f}_{0,x}$	$\Delta\hat{f}_x$
Value	1.2	2.0	0.85	0.75	0.144	0.064	0.288	0.128

5. Numerical simulations with the non-linear structural riser model

The main objective of this section is to evaluate prediction performances of time domain VIV model with respect to the results of 3D current VIV. The results of tests and simulations with non-linear riser models, NLM were compared for all geometries.

5.1. VIV induced tension fluctuations and mean tension

Tension statistics at the riser top would be one of the criteria for identifying the trend of VIV. When the current acts on the riser, the top tension not only increases due to the drag forces but also fluctuates by the VIV responses. For a tensioned beam with one pinned and one free end, vibrations in the axial direction are induced due to coupling with the transverse VIV motions. The vibration occurs twice for one period of cross-flow or in-line. When the frequency of cross-flow and in-line are ω and 2ω, the frequencies of the axial vibration for each

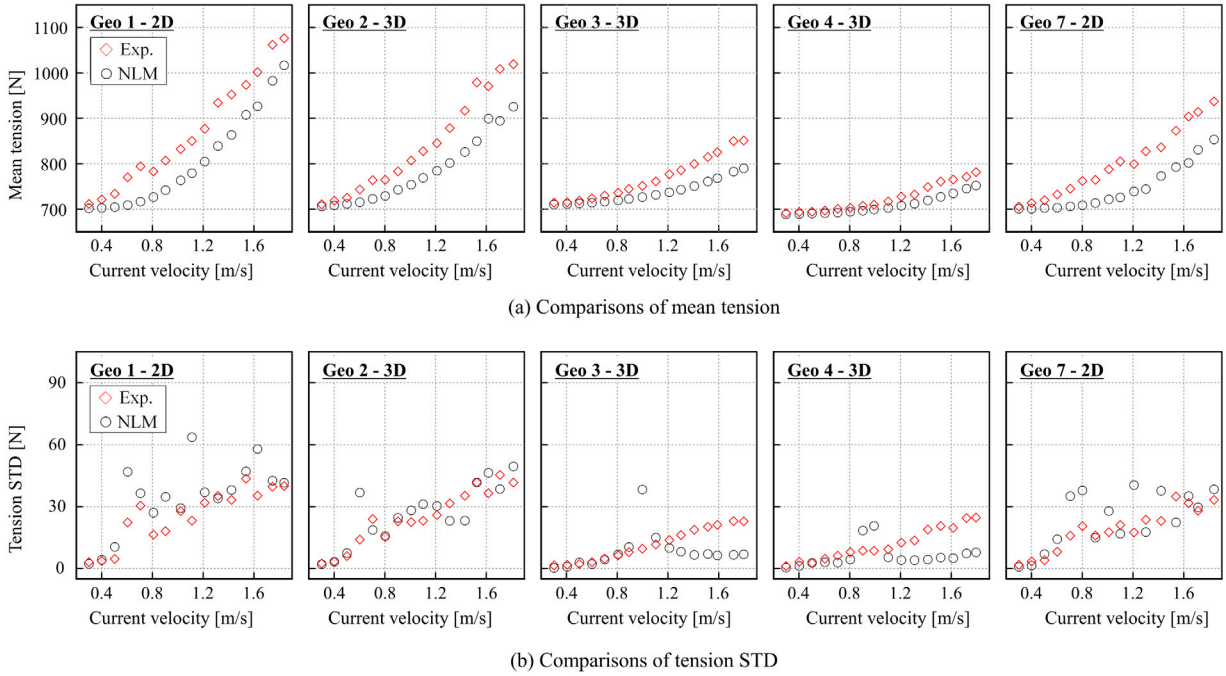

(a) Comparisons of mean tension

(b) Comparisons of tension STD

Fig. 9. Comparison of the mean tension and tension STD at the top of the riser.

VIV response become 2ω and 4ω. The vibrations can be formulated as follows (Huse et al., 1999):

$$T(z,t) = \frac{1}{4} m_z x_0^2 k^2 \omega^2 L^2 \left(1 - \left(\frac{z}{L}\right)^2\right) \cos(2\omega t) \tag{10}$$

where, x_0, ω, and k are the amplitude of VIV, the frequency of VIV, and the wavenumber of vibration. L, z, and m_z are the length of the riser, z coordinate, and the mass per unit length, respectively. ; $T(z,t)$ is the tension as a function of coordinate, z and time, t.

In order to compare the tension statistics between the simulation and test, the mean and standard deviations (STD) of the top tension were compared according to the current velocity and geometry as shown in Fig. 9. As shown in Fig. 9a, the mean tensions for all geometries increase as the current velocity gets higher due to the increase of the drag forces. The simulations generally underestimated the test results, however, the differences in mean tension between the tests and simulations were within 10% for all the cases. The difference might be due to lower drag forces in the simulations. The drag coefficient, C_D was set to 1.2 which is a preferred value for a vertical cylinder. In terms of the current profiles types, Geo 3 and Geo 4 of among the 3D current profile cases give a smaller mean tension than the 2D current profile cases (Geo 1 and Geo 2) for both tests and simulations. The mean tension levels of Geo 2 were lower than Geo 1 and higher than Geo 7. This was because the effective current velocities which are normal to the riser (in relation to the inclination angle of the riser, τ,) were getting lower when the 3D level of the current profile increases.

Tension STD comparison results are shown in Fig. 9b. The tension STD is proportional to the square of the VIV amplitude by Eq. (10). As seen in the results, for 2D current cases (Geo 1 and Geo 7), the results of STDs showed relatively larger STDs compared to 3D current (Geo 3 and Geo 4) current for both simulations and tests. Among the 3D current profile cases, only Geo 2 showed a similar level as observed for the 2D current profile cases both for the tests and simulations. This might be due to not only decreased effective current velocity but also the unstable VIV responses. When VIV amplitudes are large and stable, higher tension STDs are expected. However, as the 3D level of the current profile increases in terms of Shearedness and Directionality, the number of the VIV modes participating in responses increases. So, the VIV response in 3D currents would be irregular and smaller than 2D current profiles cases. In comparisons for the tests and simulations, the STDs of the simulations were normally rather larger than the results of the test results for Geo 1, Geo 2, and Geo 7. However, the tests of Geo 3 and Geo 4 were somewhat underestimated, especially for higher current velocity cases. This implies that the time domain VIV model has a prediction uncertainty for higher current velocities for 3D current profiles at high Directionality and Shearedness.

In specific cases, the frequency of the axial vibrations may coincide with the eigenfrequency of the first mode in the axial direction of the riser. The resonance can be caused by both cross-flow and in-line, and the current velocity that causes the axial resonance is referred to as a critical velocity. Axial resonance may occur when a critical flow velocity is reached, which can be estimated as follows (Huse et al., 1999):

$$V_{c,IL} = \frac{cD}{16StL} \tag{11}$$

$$V_{c,CF} = \frac{cD}{8StL} \tag{12}$$

where, the $V_{c,CF}$ and $V_{c,IL}$ are the critical flow speeds associated with axial vibration frequency caused by CF and IL VIV responses, respectively. c is the velocity of sound in the material of the riser and D is the diameter of the riser.

For 2D current profile cases, the axial resonances were clearly observed as seen in Fig. 9b. For Geo 1 and Geo 7, the critical velocities of CF and IL ($V_{c,CF}$ and $V_{c,IL}$) were about 0.6 to 0.8 m/s and 1.4 to 1.6 m/s, respectively. The axial resonances are identified by the large tension STD in Fig. 9b. , also, they can also be observed outside the critical velocity range depending on the mode shifting and the stability of the VIV response. For the 3D current profile cases, the axial resonances were rarely observed for simulation and test due to unstable and small VIV amplitudes. This implies that the probability of axial resonances in the 3D currents is lower than for the cases with 2D current profiles.

5.2. VIV displacement and trajectory

In order to compare the VIV responses along the riser, the STD of the CF and IL displacements were calculated at each cross-section and plotted as a function of z coordinate of the riser. The STD of displacements

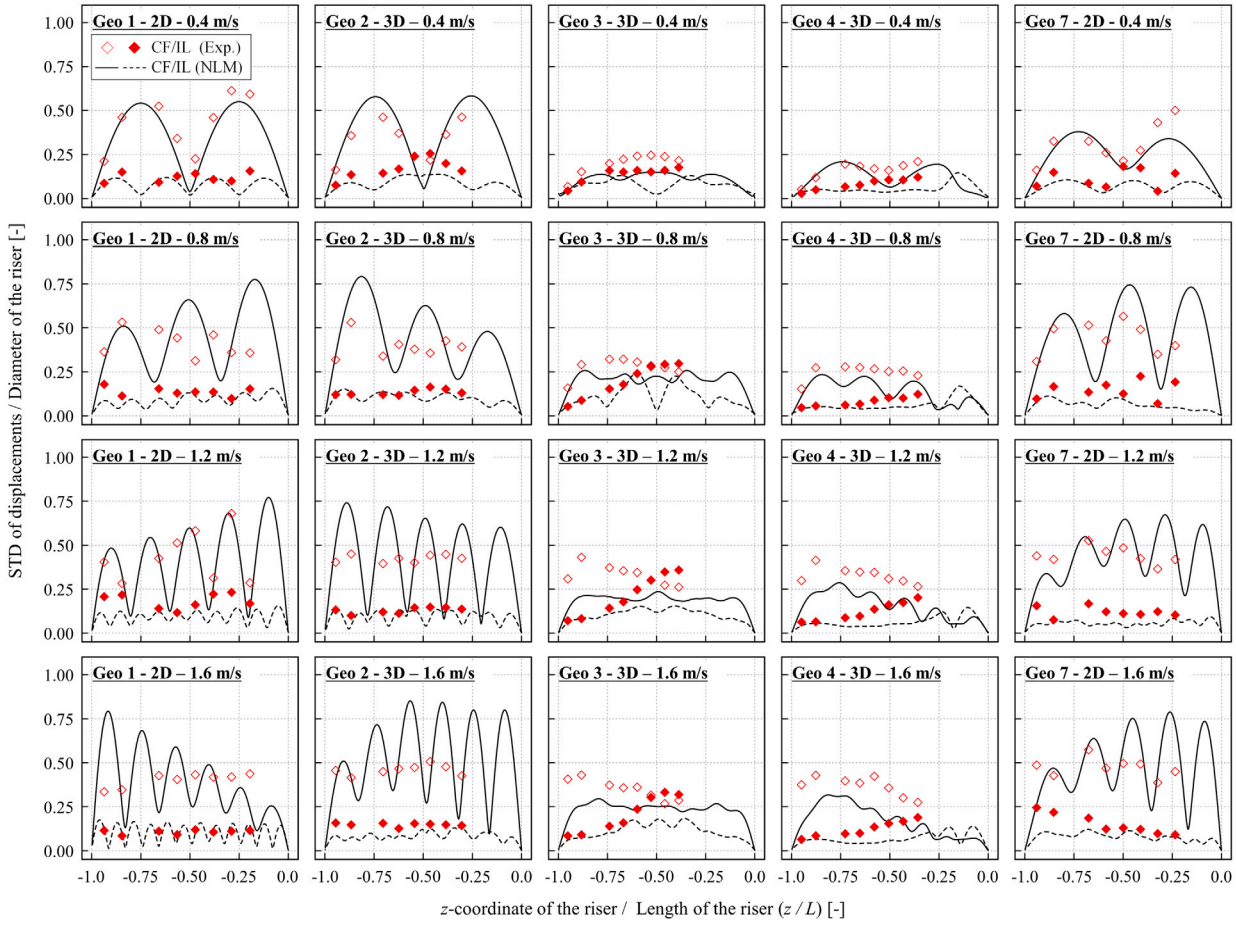

Fig. 10. Comparison of the displacement profiles along the riser length ($U = 0.4$ m/s, 0.8 m/s, 1.2 m/s, 1.6 m/s, $z/L = 0.0$ — Top of the riser, $z/L = -1.0$ — Bottom of the riser).

and z coordinate of each cross-section were non-dimensionalized with the riser diameter, D_e, and the riser length L, respectively. The results for several velocities of simulations and tests are shown in Fig. 10.

As seen in the results, simulations well predicted the test results for 2D uniform and shear flow (Geo 1 and Geo 7) regardless of the current velocity. But the in-line responses of simulations were slightly underestimated in 2D shear flow, and these results coincided with the previous study results by Drengsrud (2019). When it comes to 3D current profile cases, the simulations results of Geo 2 also showed good agreements with the test regardless of current velocities and response type. But 3D current cases with higher Directionality and Shearedness (Geo 3 and Geo 4), simulations underestimated the results for cross-flow and in-line responses, especially at higher current velocities as seen at 1.2 m/s and 1.6 m/s. Underestimation results for Goe 3 and Geo 4 coincided with the trends of tension STDs in Section 5.1. Also, the definitions of the cross-flow and in-line for 3D current profiles were rather unclear due to chaotic response regardless of CF and IL in experiments and simulations. The profiles of VIV responses of Geo 3 were too flat to distinguish the mode order. Also, the local CF and IL of the test were suspected to be switched between each other in the riser location range $z/L = -0.5$ and $z/L = -0.25$. This indicates that the VIV responses along the riser were too chaotic. In the case of Geo 4, despite higher Directionality and Shearedness than Geo 3, it was easier to identify the mode order and direction of local CF and IL.

To investigate the detailed features of VIV responses for 3D current profile cases, the trajectories according to the riser length and contour plot of displacement of CF are plotted in Fig. 11 for the maximum current velocity cases of Geo 2, Geo 3, and Geo 4. Trajectories of VIV were non-dimensionalized with the riser diameter, D_e, and the contour plot represents the displacement level of cross-flow in time along the non-dimensionalized riser length (z/L) as a color map.

The current profiles of Geo 2 and Geo 3 are symmetric to the middle point along the riser length (i.e global x–z plane) in Fig. 3a (Section 2.2). Two dominant excitation modes at both ends of the riser would be developed in different directions. For Geo 2, the angle differences between modes in the global x–y plane were not enough large so that one excitation mode dominated another as seen in Fig. 11a. Because of that, even in 3D current profile, the VIV responses of Geo 2 were relatively stable along the riser as seen in Fig. 11b. In the case of Geo 3, excitation modes near the bottom and top are clearly separated due to high Directionality as illustrated in Fig. 11a. When the two modes were crossing at the midpoint, the responses would become chaotic due to different direction of modes with similar strength as shown in Fig. 11b. While the current profile of Geo 4 is an asymmetric profile relative to the center of the riser due to the high Shearedness, the excitation mode which was developed near the bottom was more dominant than the excitation mode near the top. The responses were therefore less chaotic than for Geo 3 near the midpoint, whereas responses became unstable between the top and midpoint of the riser as shown in Fig. 11b. In summary, the number of dominant modes and their relative spatial distributions determines the chaotic level of VIV responses, and it is not easy to characterize the chaotic level in terms of Directionality and Shearedness. Although the amplitude predictions were slightly different, the simulations also could reflect the response characteristics in 3D currents.

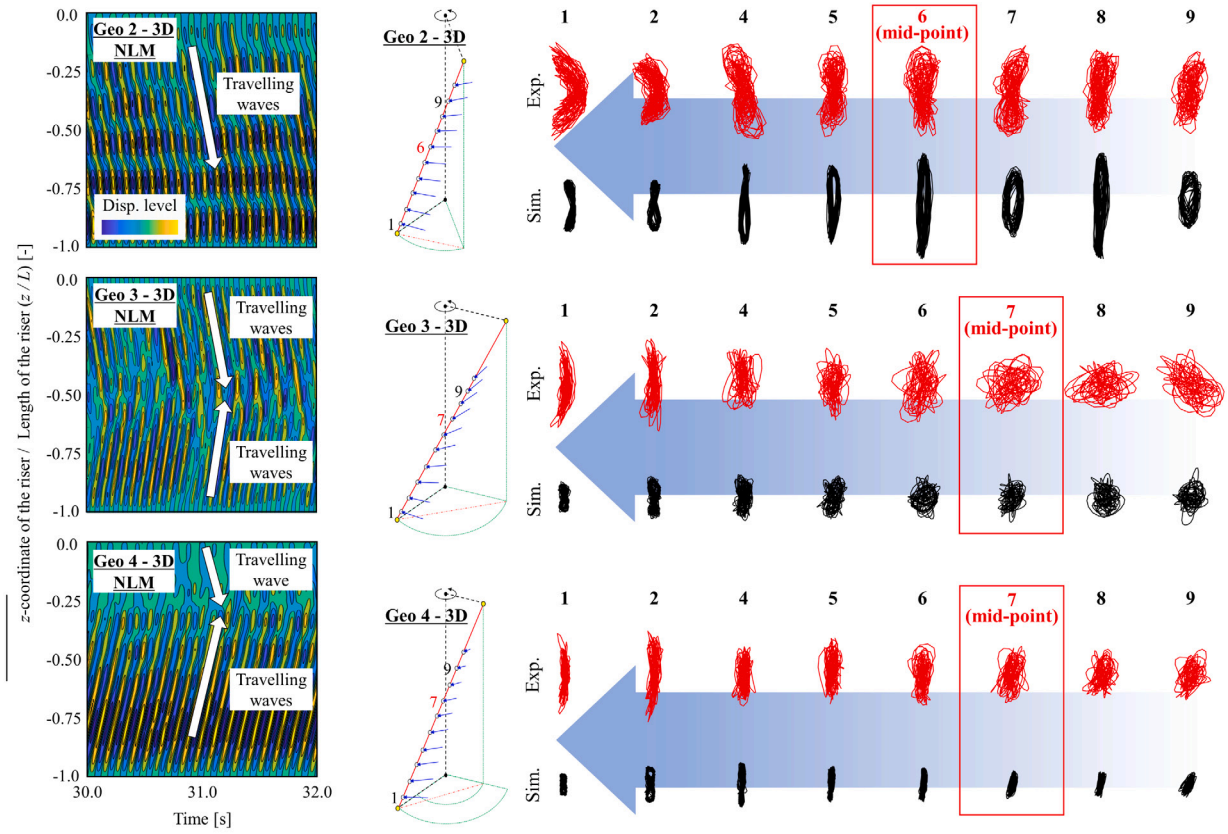

(a) Contour plot of displacement (CF)

(b) VIV trajectories of tests and simulations along the riser length

Fig. 11. Illustration of VIV responses for 3D current profile cases (U = 1.6 m/s, z/L = 0.0 — Top of the riser, z/L = −1.0 — Bottom of the riser).

5.3. Dominating frequency and acceleration spectrum

The dominating frequency of VIV is an important quantity for the VIV predictions. The dominating frequencies of the cross-flow and in-line were defined as the peak frequency of the acceleration spectra of the local cross-flow and in-line natives. Except for Geo 1, the dominating frequency could vary along the length of the riser due to the variation of the current along the riser length. Near the bottom and midpoint of the riser were considered for the comparisons of the dominating frequencies. Locations near the bottom and midpoint of the riser were considered for the comparisons of the dominating frequencies. Near the bottom of the riser, mode competition is less pronounced than for other locations due to higher current velocity. Whereas, in the middle of the riser, the current velocity is reduced implying that several modes competing. The results are shown in Fig. 12 according to location, current velocity, and Geometry.

For 2D current profile cases (Geo 1 and Geo 7), the tests and simulations showed good agreements regardless of the current velocities, locations, and response types. This means that the proposed synchronization parameters are well defined. On the other hand, the case of 3D current profiles showed differences according to each geometry. In the case of Geo 4, the test results were well predicted for both near the bottom and midpoint of the riser. For Geo 2 and Geo 3, simulation results showed small deviations from the tests at the bottom of the riser. At the midpoint of the riser, the results of Geo 2 showed good agreements while some of the cases showed that the local cross-flow and in-line were switched. Especially, local cross-flow and in-line of Geo 3 were not easy to distinguish at the midpoint of the riser regardless of the test and simulations. The switched dominating frequencies were due to the chaotic VIV response at the midpoint of the riser, which can be related to the location and direction of the excitation modes.

In order to investigate the energy distributions of the VIV responses in the frequency domain, spectrum comparisons were considered. The local in-line and cross-flow signals at the bottom and midpoint of the riser were transformed as the acceleration power spectral density (PSD), and the PSD were scaled by the square root of the ACC PSD for easier comparisons. The spectra are plotted in Fig. 13.

As shown in Fig. 13a, at the bottom of the riser, the PSD of in-line and cross-flow were clearly distinguished for all geometries, and the PSD of 3D current cases were wider than those of 2D flow, especially Geo 3 and Geo 4. The results indicated that lots of excitation modes with different frequencies as well as a dominating mode participated in the VIV responses of 3D current cases. Simulations also showed a similar trend as the experiments, but for all geometries, narrowband spectra were observed compared to tests. The reason would be due to the variation in the natural frequency in time due to the differences in tension fluctuations and the disturbances of the fluid in the test basin. The flow disturbances were minimized by the process strategy, but not completely. This might result in a wider spectrum bandwidth of experiments. In addition, for Geo 3 and Geo 4, the narrow area of the simulation PSD was consistent with the fact that the amplitudes of simulations were smaller than that of tests as discussed in Section 5.2. On the other hand, As seen in Fig. 13b, VIV responses of the 2D and 3D current profile cases were clearly different near the midpoint of the riser. For the PSD of the tests, the energy distributions were quite much wider for the bottom cases. Especially for the 3D current cases, the width of the cross-flow PSD was similar to that of in-line PSD. In the case of Geo 3 test, not only the width of PSD but also the energy level of CF and IL were similar to each other, so in-line and cross-flow were not easy to distinguish as discussed in Section 5.2. For the simulations, the width of PSD of 3D flow was considerably wider than that of 2D flow near the midpoint of the riser.

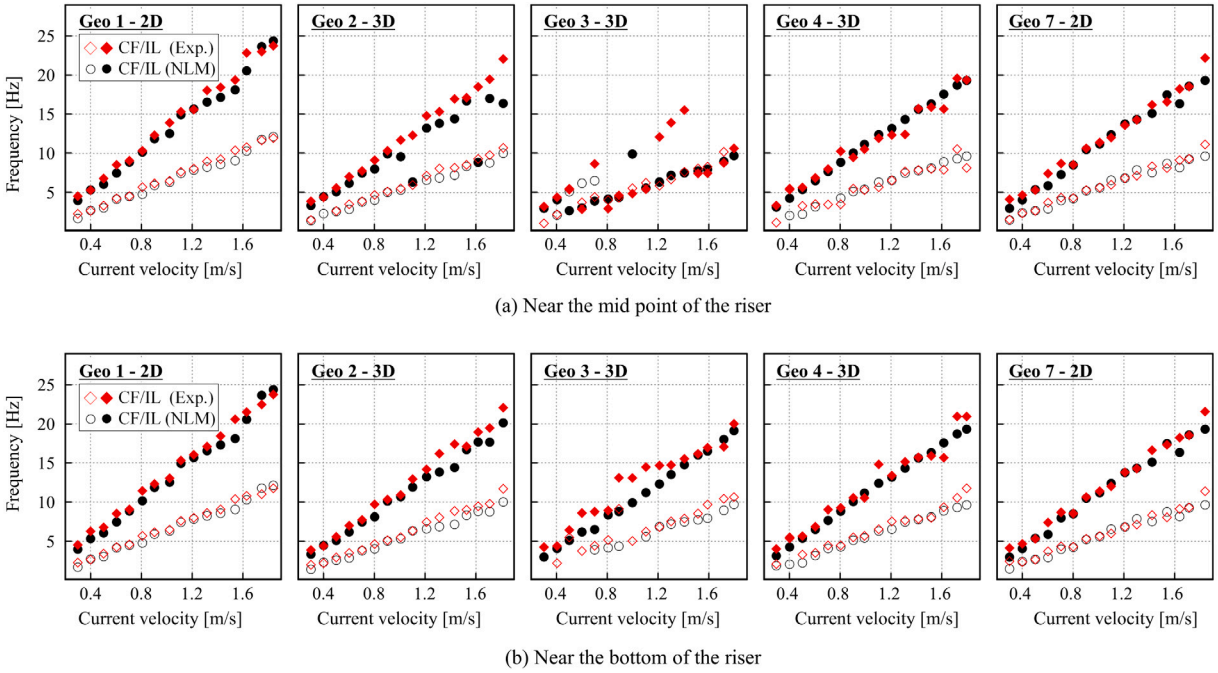

Fig. 12. Comparison of the dominating frequencies of CF and IL at the different points of the riser.

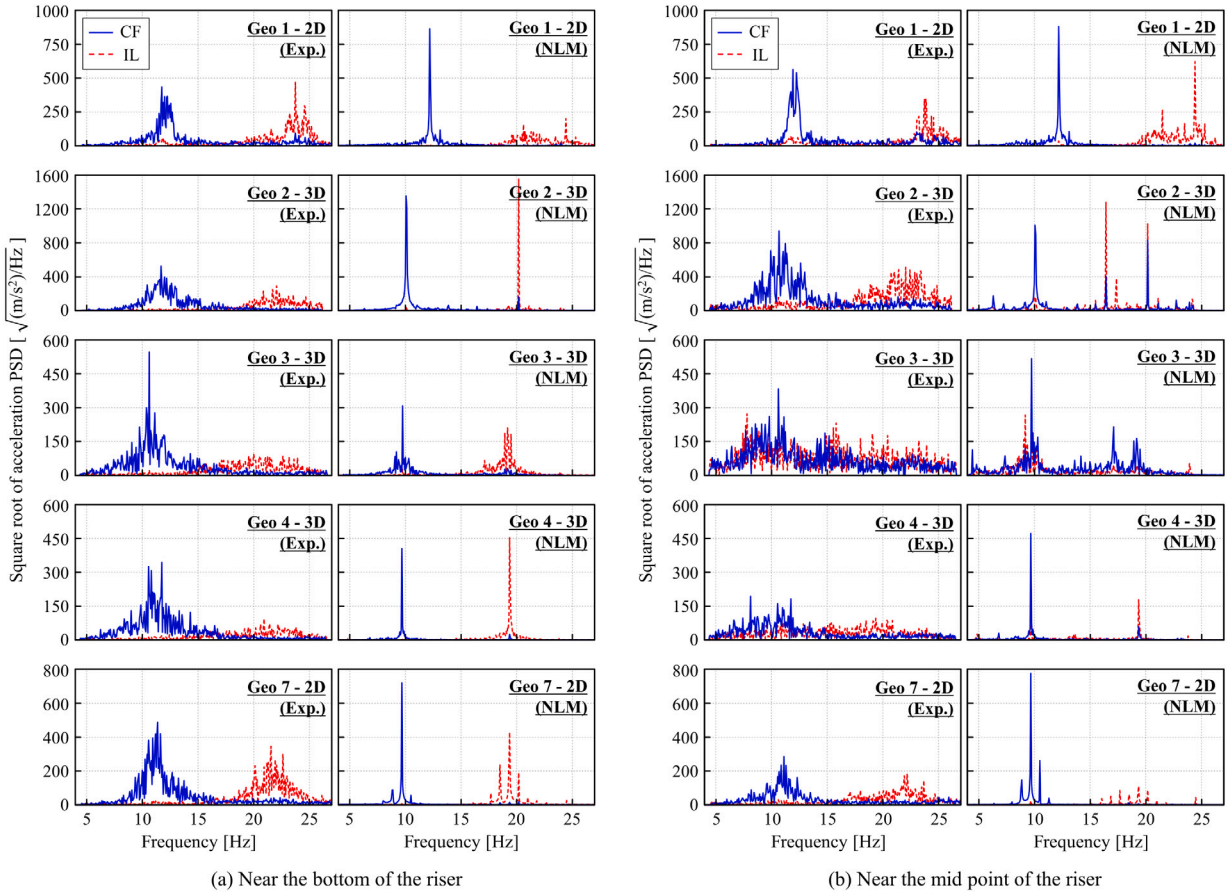

Fig. 13. Comparison of the PSDs of CF and IL at the different points of the riser (U = 1.8 m/s, Maximum current velocity).

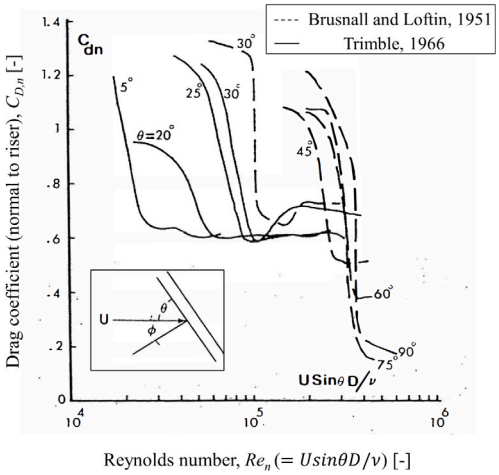

Fig. 14. Normal drag coefficient versus Normal component of Reynolds number for inclined cylinders (by Sarpkaya and Isaacson (1981)).

6. Discussion on empirical parameters for 3D current VIV

6.1. The drag coefficient of inclined cylinder

In Section 5, it was shown that the VIV responses of the simulations were underestimated for high levels of 3D current profiles. However, the frequency predictions showed a good correlation with the test results regardless of conditions. The underestimation might be due to the higher hydrodynamic damping in the system, while the synchronization model and the frequency parameters are still valid. One noteworthy fact is that earlier studies of an inclined cylinder showed the effect of the flow attack angle on the drag coefficient. An illustration of the drag coefficient as a function of the inclination angle of the cylinder and of the Reynolds number was provided by Sarpkaya and Isaacson (Sarpkaya and Isaacson, 1981). The results are seen in Fig. 14. In Fig. 14, θ is the same as τ in this paper.

As can be seen from the results, the drag coefficient can vary depending on Reynolds number and the inclined angle of the riser. The present hydrodynamic coefficients had been mainly optimized for the vertical riser in 2D flow (Thorsen et al., 2017; Ulveseter et al., 2018, 2019), and there was no consideration of such effects. The inclination angle of the rotating rig test riser, τ, in the static configuration is 50.7° for Geo 3 and 58.3° for Geo 4. In a dynamic analysis, the inclination angle of the riser will be smaller as the static displacement increase by the drag forces. Even though the τ is known in the static analysis stage, it is not easy to apply to the above tests result in the simulations. This is because the slope of all elements of the riser and the current velocity normal to the riser would vary as a function of time and space during the dynamic analysis.

The hydrodynamic coefficient of the proposed time domain VIV model is currently neglecting the Reynolds number effect due to the lack of test data. Also, the drag force term in the load model (refer to Eq. (3)) will mainly contribute to the hydrodynamic damping. Therefore, although the drag coefficient is correlated with $C_{v,x}$ and $C_{v,y}$, only the influence of the drag coefficient on the VIV response was investigated. In a previous study, it was demonstrated that a lower drag coefficient will imply higher VIV response levels for cases corresponding to tilted riser flow conditions (Kim et al., 2021a).

6.2. Drag coefficient sensitivity for displacements

As seen in Fig. 14, the drag coefficients can vary from 1.2 to 0.6 depending on the Reynolds number, and both in-line and cross-flow responses would be amplified as the drag coefficient is decreased. In order to investigate the VIV response to drag coefficients changes, numerical simulations with NLM were performed for Geo 3 and Geo 4. In Fig. 15, displacement STD profiles are illustrated according to drag coefficients and current velocities.

Fig. 15 shows cross-flow and in-line displacement results with a drag coefficient of 1.2 and 0.6. For Geo 3, the simulations with a drag coefficient of 0.6, the cross-flow responses of simulations were amplified according to test results, and in-line responses were larger than that of the test. For simulations of Geo 4, lowering the drag from 1.2 to 0.6 resulted in excessive amplification of the displacement even in a low current velocity. For higher current velocities, cross-flow responses were over-amplified and the in-line responses were at a similar level as the experiment. The characteristics of the VIV response were not changed even if the drag coefficient is changed. For example, mode shape and mode number were still the same regardless of the drag coefficient.

7. Case study on VIV fatigue damage due to 3D current

Sections 5 and 6 focused on the evaluation of the time domain VIV model with respect to the 3D current VIV. On the other hand, the main interest for the riser design would be the fatigue damage by the VIV-induced bending. The main purpose of this section is to compare riser fatigue analysis results according to the method of structural modeling of the riser and current profile, based on the case study. Several points should be noted for the VIV fatigue analysis of the Rotating rig test riser:

- The test riser was made by a rubber hose equipped with a steel wire insert to provide high axial stiffness and allow for pretension while the bending stiffness was kept low, thus obtaining a tension dominated riser. Due to the non-isotropic stiffness, only the bending stresses at the outer fiber of the rubber were applied in the stress analysis to investigate how different modeling methods behaved relative to each other with respect to fatigue.
- In the previous section, it was shown that the current parameter set gave some underestimation in VIV prediction for Geo 3 and Geo 4. However, in this section, the present empirical parameters were applied for all modeling methods, since the focus was on the comparison of fatigue damages between different modeling methods relative to each other.
- Since the stiffness of the riser is dominated by tension, the ratio of IL's amplitude and CF's amplitude is larger than that of bending stiffness dominated risers (Baarholm et al., 2006). In this case, the highest fatigue damage may not occur in the CF direction. Moreover, it is important to include IL loads in 3D current conditions, where local IL and CF response directions may vary.

The bending stresses by the VIV-induced bending moments can be formulated as in Eq. (13), and the relevant terms and coordinated system are illustrated in Fig. 16.

$$\sigma_z(\theta,t) = \frac{M_x(t)}{2I_{xx}} D_e \sin\theta + \frac{M_y(t)}{2I_{yy}} D_e \cos\theta \tag{13}$$

where, the $\sigma_z(\theta,t)$ is the bending stress, and I is the moment of inertia with respect to the axis. $M_x(t)$ and $M_y(t)$ are the bending moments induced by the cross-flow and in-line vibrations, respectively.

The stresses were calculated at 16 points around the circumference of each cross-section. With the bending stress as input, the fatigue analysis was performed with WAFO based on the rainflow counting method (Brodtkorb et al., 2000). In terms of the S–N curve, the material constant was 11.687, and the slope of the S–N curve was 3. Among the calculated fatigue damages for 16 points around the cross-section, the maximum value was designated as the fatigue damage, $D_{fat,i}$ of the ith cross-section. The results of the fatigue damage calculation were transformed into yearly fatigue damage.

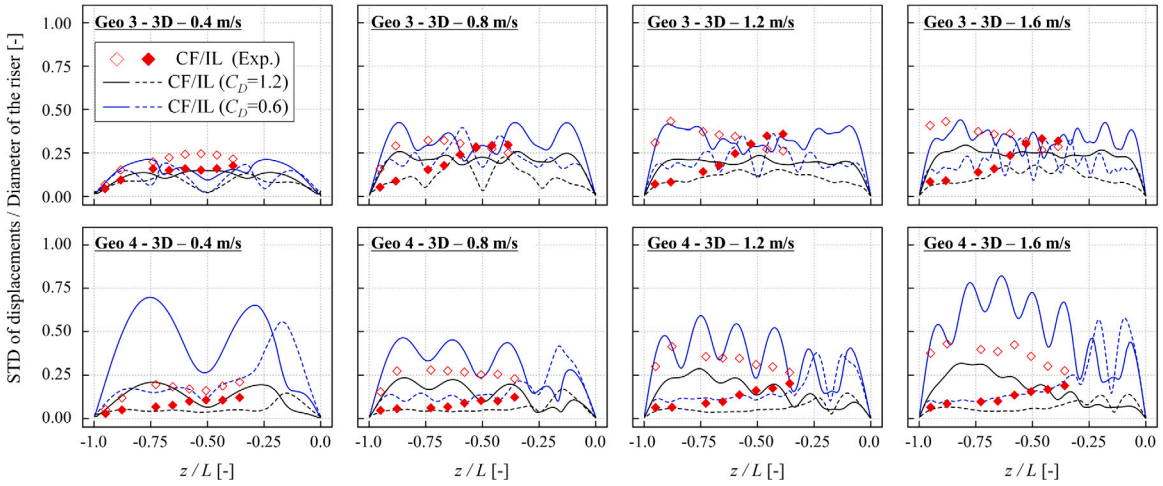

Fig. 15. Drag coefficient sensitivity results of Displacement STD profiles.

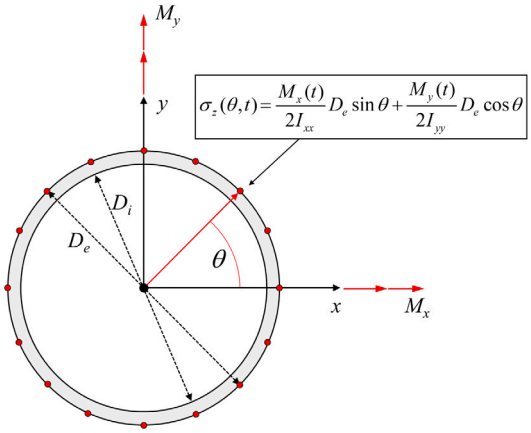

Fig. 16. Coordinate system for computation of VIV induced bending stresses.

7.1. Spatial distributions of fatigue damage

To compare the spatial distributions of fatigue damage along the riser, the fatigue damage profiles are plotted as a function of non-dimensionalized riser length, z/L in Fig. 17 according to each geometry, the riser modeling method, and current velocity.

As seen in Fig. 17a, for Geo 2 with a lower level of 3D current, deviations in dominating mode order and mode shape between NLM, LM, and LU were small regardless of current velocity. The locations of maximum fatigue damage for each method were also similar to each other, and the responses for all cases were dominated by the standing waves. Exceptionally, at 0.8 m/s of current velocity, NLM showed the lowest fatigue damage, and this would be because the responses were unstable and decreasing due to the axial resonance. Also, as shown Fig. 17a at 1.2 m/s, the fatigue damage obtained by application of LU was underestimated compared to other methods. This was because strong shifts between the modes that were participating occurred.

In the case of NLM and LM for Geo 3, at both ends of the riser, two different dominating modes were developed with different directions relative to the riser axis. The excitation modes of LU were developed and located in the same plane. As a result, for NLM and LM, the maximum fatigue damages were observed at both ends while the maximum fatigue damages of LU were observed in the middle section of the riser due to the symmetric mode shape and current profiles. Although all of the methods showed symmetric fatigue damage profiles, the shape of NLM and LM were definitely different from that of LU as shown in Fig. 17b. In addition, the LM and NLM were dominated by the traveling waves, while LU was dominated by the standing waves.

When it comes to Geo 4, the results showed different trends from Geo 2 and Geo 3. Due to the asymmetric current profiles, the dominating mode was observed near the bottom of the riser where the maximum current is acting for all methods. Dominating modes of NLM and LM were interfering less with other modes because of different attack angles to the riser. On the contrary, the dominating modes of LU competed with each other in the same plane. As seen in 17c, the fatigue damages of LU were more spread along the riser length at all current velocities. Fatigue damages of LM were similar to NLM, but another difference was the maximum fatigue damage location due to different boundary conditions.

Contour plots were introduced to investigate differences in the location of the maximum fatigue damage over the entire velocity range. The color represents the fatigue damage, and the x and y-axis indicate the current velocity and non-dimensionalized coordinate, respectively. The plots were separated into low and high current velocity intervals for each geometry. The results are illustrated in Fig. 18.

As shown in Fig. 18a, the noticeable difference between the modeling methods for Geo 2 was the position of the maximum fatigue damage. The location of the maximum fatigue damage was near the top of the riser for LU and LM while the maximum results of NLM were observed near the bottom of the riser. This was because the VIV-induced tension fluctuations disturbed the VIV response resulting in lower bending stress near the top of the riser for the analysis based on NLM. In contrast, at a similar location, the VIV-induced tension fluctuations are almost eliminated for the linear structural model resulting in higher bending stresses than those obtained from the NLM.

In the case of Geo 3, as seen in Fig. 18b, NLM showed a similar level of fatigue damages near both ends of the riser at the lower current velocity. The maximum fatigue damages of LM were almost the same regardless of the locations. On the other hand, for LU the maximum fatigue damage occurred near the middle section of the riser. The locations of the maximum fatigue damage were slightly different as the current speed increased, see Fig. 18b. The maximum fatigue damage based on the LU were still observed near the middle of the riser. The maximum fatigue damage based on the NLM was located near the bottom of the riser. Although similar strength dominating modes were developed at both ends, the dominating mode close to the top was weaker than the dominating mode near the bottom due to the bending moment decrease caused by the tension fluctuations at the top. For LM, the separations of the dominating mode near both ends of the riser were not as strong as for NLM, so the maximum fatigue damages of LM were located in the intermediate location of results for LU and NLM. When it comes to Geo 4, as shown in Fig. 18c, there were

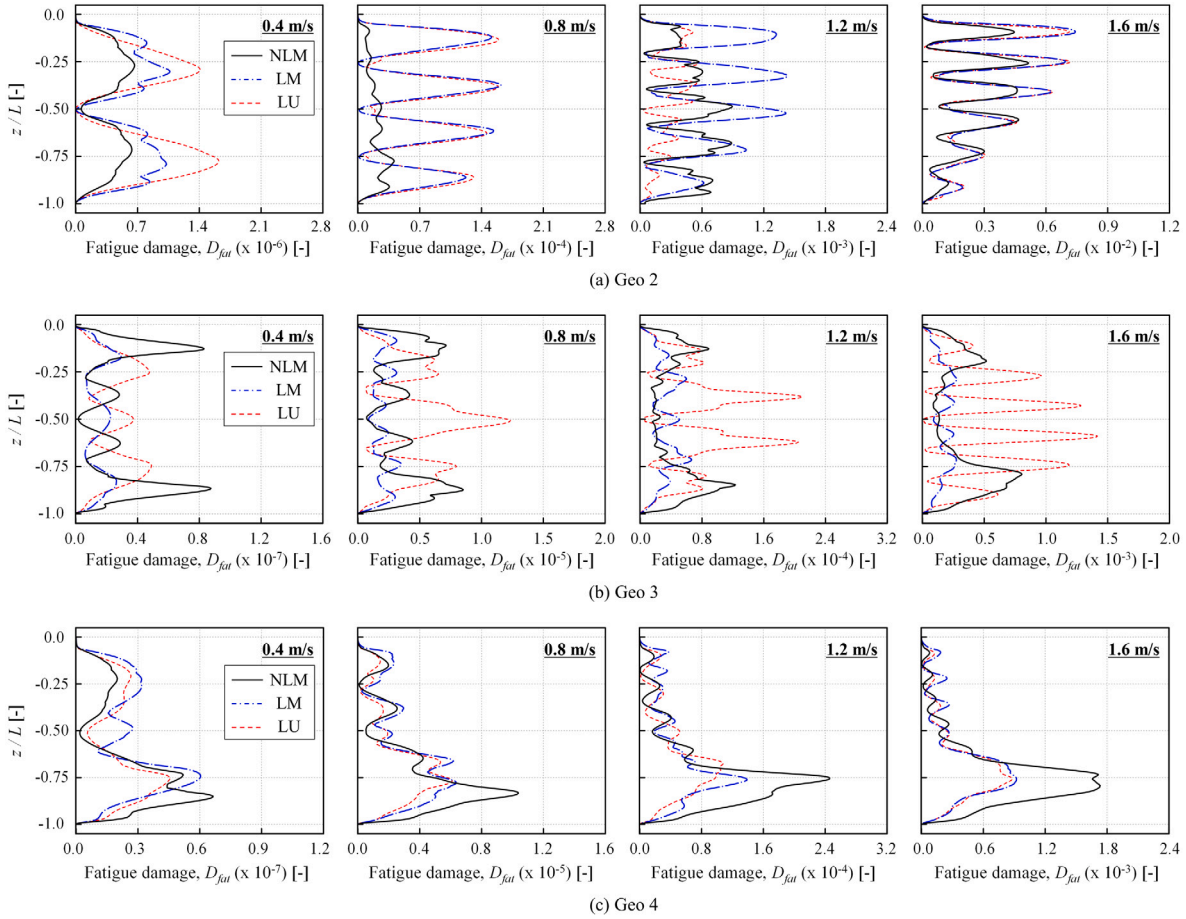

Fig. 17. Comparison of the fatigue damage profiles for each Geometry ($U = 0.4$ m/s, 0.8 m/s, 1.2 m/s, 1.6 m/s, $z/L = 0.0$ — Top of the riser, $z/L = -1.0$ — Bottom of the riser).

no significant differences in the maximum fatigue damage locations between the different methods.

7.2. Maximum fatigue damage comparison

The maximum fatigue damage along the length of the riser, $D_{fat,max}$ is one of the key results to be checked in riser design (DNV.GL, 2017). In order to compare maximum fatigue damages from the viewpoint of the riser design, the maximum fatigue damage of LU, D_{fat,max_LU} was designated as the reference fatigue damage. This was because the LU is the conventional method for VIV analysis based on the frequency domain approach. A comparison of the maximum fatigue damage obtained by application of the different methods is shown in Fig. 19 expressed in terms of the fatigue damage in logarithmic scale and the fatigue ratio. Data points located below the red line (which corresponds to a factor of one) in Fig. 19b, indicates that the maximum fatigue damage of LU at a given current velocity is higher than the corresponding value obtained by application of LNM or LM.

As seen in Fig. 19, the results varied depending on the geometry. For Geo 2, the maximum fatigue damages of LU were mostly higher than the results of NLM and LM. A few cases showed the opposite results with a factor of 3, which was found to be due to a strong shifting of modes. In the case of Geo 3 with higher Directionality than Geo 2, the fatigue damage profile of LU was different from LM and NLM as discussed in Section 6.1. The LU was dominated by the standing waves while LM and NLM were dominated by the traveling waves. The responses of LU were relatively stable and higher than LM and NLM, and the conservatism of LU is higher than for Geo 2.

In the cases of Geo 4, the trends clearly differed from Geo 2 and Geo 3 where the NLM is more conservative than other methods by a factor of 3 or less. Due to the current profiles with high Shearedness of Geo 4, each active mode and its excitation zone were separated. Therefore, the dominating mode of NLM is relatively free from the mode competition compared to that of LU. For this type of current profile, LU could be non-conservative.

8. Conclusions

In the present study, VIV responses in 3D currents have been investigated by time domain VIV numerical simulations. The main results of the validation for the rotating rig test data are as follows:

- With respect to VIV dominating frequency, the simulations agreed quite well with the experimental data for three-dimensional current profiles as well as two-dimensional flow current profiles.
- In terms of the VIV induced tension fluctuations at the top of the riser and VIV responses, the test data were well predicted by simulation for 2D currents. However, for 3D current with a high Shearedness and Directionality, VIV displacements were underestimated at high current velocities.
- Based on the fact that the drag coefficient could be reduced due to the riser's inclination angle, a drag coefficient sensitivity for the VIV response was investigated for cases with 3D current profiles. The results showed that the VIV responses could be amplified due to reduced hydrodynamic damping for a lower drag coefficient.

The fatigues damages caused by VIV bending stress were compared between different modeling methods for both the riser and current profiles. The main observations are as follows:

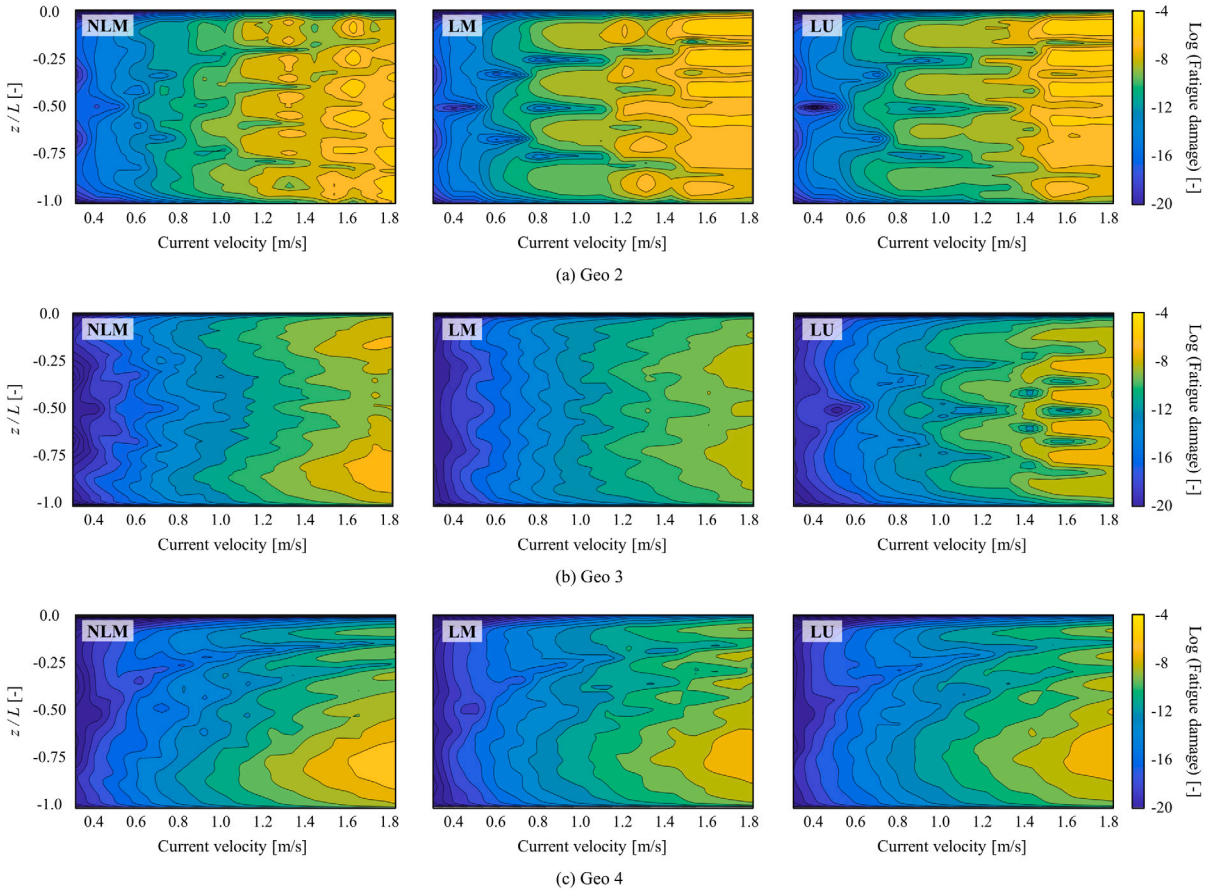

Fig. 18. Colormap of the fatigue damage as a function of current velocity and z/L (Geo 2: (a), Geo 3: (b), Geo 4: (c)).

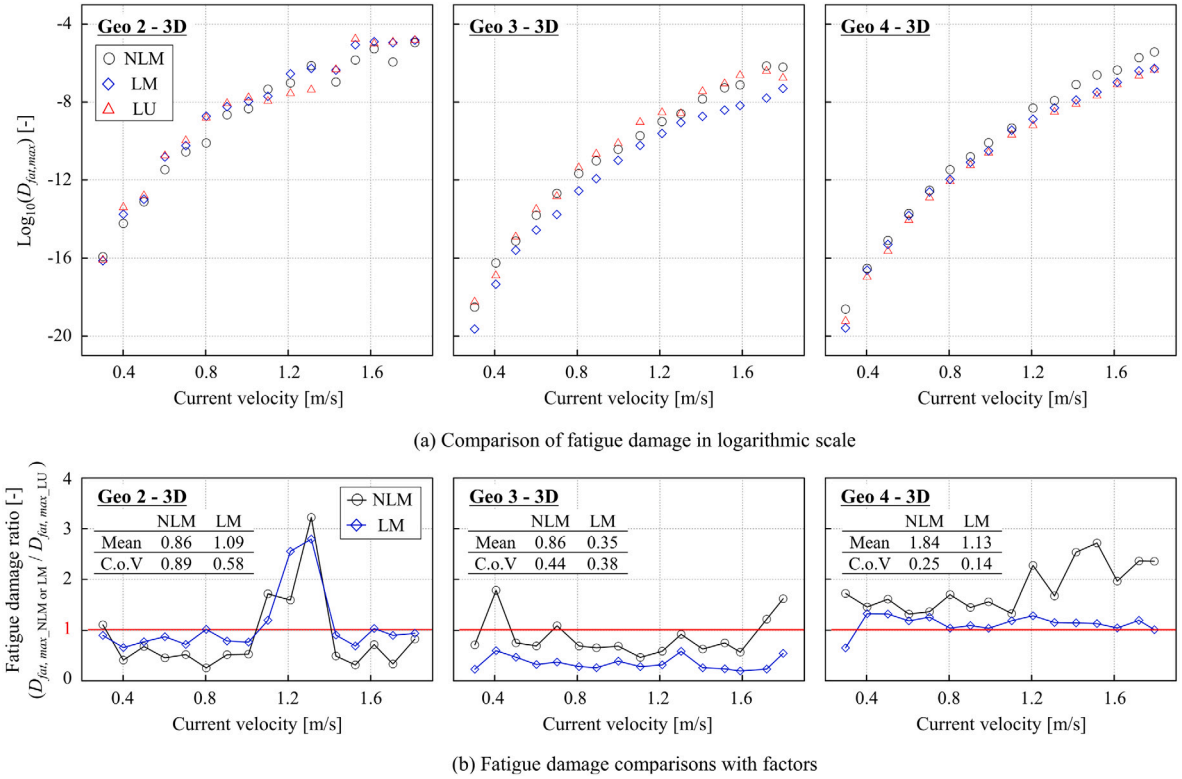

Fig. 19. Comparison of the maximum fatigue damages between NLM, LM, and LU with factors (Red line in (b) corresponds to LU results).

- Between the linear and nonlinear structural riser model, the different eigenmode shapes due to the different boundary conditions resulted in different fatigue damage profiles when subjected to the 3D current profiles. The VIV-induced tension fluctuations also affected the VIV stability and location of the maximum fatigue damage.
- The fatigue damages due to VIV induced by three-dimensional current depend highly on how much the dominating VIV modes interfere with other candidate modes in terms of the directions relative to the riser and on the locations along the riser. In this respect, prediction using a uni-directional current profile does not always guarantee conservative fatigue damage estimates.
- The fatigue damage estimates based on NLM, which represents the test set-up in the best way, show deviations from those obtained by application of LU which corresponds to industry practice. This indicates that VIV design practices can be improved by application of the NLM approach. However, it should be noted that the test riser was manufactured by rubber with a pre-tensioned steel wire insert to obtain relevant modes for the test. Therefore, the fatigue damage caused by axial vibration was not considered in this study.

In conclusion, the applicability of the time domain VIV model to the 3D current VIV was demonstrated, and the time domain model was able to represent structural nonlinearity (i.e., tension variations) when experiencing VIV. In addition, from a fatigue design perspective, it was shown that the conventional VIV fatigue design method for 3D currents may differ from the fatigue damage of more refined structural models of the riser. Application of the VIV model within the context of riser design requires optimization of empirical hydrodynamic coefficients, and there are uncertainties in the hydrodynamic coefficients especially for risers subjected to complex flow conditions, which need to be further reduced. Also, VIV analysis studies of more complex structural models than the models applied in the present study are required.

CRediT authorship contribution statement

Sang Woo Kim: Conceptualization, Methodology, Software, Formal analysis, Investigation, Data curation, Writing – original draft & editing, Writing – review & editing, Visualization, Validation. **Svein Sævik:** Conceptualization, Methodology, Software, Validation, Investigation, Writing – original draft & editing, Writing – review & editing, Supervision, Project administration. **Jie Wu:** Conceptualization, Methodology, Validation, Investigation, Resources, Writing – original draft & editing, Writing – review & editing, Supervision, Project administration. **Bernt Johan Leira:** Methodology, Validation, Investigation, Writing – original draft & editing, Writing – review & editing, Supervision, Project administration.

Declaration of competing interest

The authors declare that they have no known competing financial interests or personal relationships that could have appeared to influence the work reported in this paper.

Acknowledgments

The authors wish to thank the Norwegian Deepwater Programme and SINTEF Ocean for allowing the use of the Rotating rig test data. We would also like to thank Mr. Halvor Lie, Dr. Elizabeth Passano, Dr. Decao Yin for valuable discussions on VIV in general.

References

Baarholm, G.S., Larsen, C.M., Lie, H., 2006. On fatigue damage accumulation from in-line and cross-flow vortex-induced vibrations on risers. J. Fluids Struct. 22 (1), 109–127.

Blevins, R.D., 1977. Flow-induced vibration, new york.

Braaten, H., Lie, H., 2005. NDP Riser High Mode VIV Tests Main Report. Technical Report, Norwegian Marine Technology Research Institute, Trondheim, Norway.

Brodtkorb, P.A., Johannesson, P., Lindgren, G., Rychlik, I., Rydén, J., Sjö, E., 2000. Wafo - a matlab toolbox for analysis of random waves and loads. In: International Offshore and Polar Engineering Conference, ISOPE-I-00-264.

Dahl, J.M., Hover, F.S., Triantafyllou, M.S., Oakley, O.H., 2010. Dual resonance in vortex-induced vibrations at subcritical and supercritical Reynolds numbers. J. Fluid Mech. 643, 395–424.

DNV.GL, 2017. Recommended Practice-F204: Riser Fatigue. Technical Report, Det Norske Veritas and Germanischer Lloyd, Oslo, Norway.

Drengsrud, H., 2019. Systematic Evaluation of VIV Prediction for Riser with Partial Strake Coverage. Norwegian University of Science and Technology, Trondheim, Norway.

Facchinetti, M.L., Langre, E.d., Biolley, F., 2004. Coupling of structure and wake oscillators in vortex-induced vibrations. J. Fluids Struct. 19 (2), 123–140.

Gabbai, R.D., Benaroya, H., 2005. An overview of modeling and experiments of vortex-induced vibration of circular cylinders. J. Sound Vib. 282 (3), 575–616.

Gao, Y., Pan, G., Meng, S., Liu, L., Jiang, Z., Zhang, Z., 2021. Time-domain prediction of the coupled cross-flow and in-line vortex-induced vibrations of a flexible cylinder using a wake oscillator model. Ocean Eng. 237, 109631.

Hartlen, R.T., Currie, I.G., 1970. Lift-oscillator model of vortex-induced vibration. J. Eng. Mech. Div. 96 (5), 577–591.

Huang, K., Chen, H.-C., Chen, C.-R., 2007. Riser VIV analysis by a CFD approach. In: International Ocean and Polar Engineering Conference, ISOPE-I-07-447.

Huse, E., 1997. Large Scale Testing of Riser Models. Main Report, Norwegian Marine Technology Research Institute.

Huse, E., Kleiven, G., Nielsen, F., 1999. VIV-induced axial vibrations in deep sea risers. In: Offshore Technology Conference, Paper NO. OTC-10932-MS.

Jhingran, V.G., 2008. Drag Amplification and Fatigue Damage in Vortex-Induced Vibrations (Ph.D. thesis). Massachusetts Institute of Technology.

Kamble, C., Chen, H.-C., 2016. 3D VIV fatigue analysis using CFD simulation for long marine risers. In: International Ocean and Polar Engineering Conference, ISOPE-I-16-320.

Kang, Z., Jia, L., 2013. An experiment study of a cylinder's two degree of freedom VIV trajectories. Ocean Eng. 70, 129–140.

Kim, S.W., Sævik, S., Wu, J., Leira, B.J., 2021a. Prediction of deepwater riser VIV with an improved time domain model including non-linear structural behavior. Ocean Eng. 236, 109508.

Kim, S.W., Sævik, S., Wu, J., Leira, B.J., 2021b. Simulating high-mode vortex-induced vibration of a riser in linearly sheared current using an empirical time-domain model. J. Offshore Mech. Arct. Eng. 143 (4).

Larsen, C.M., Lie, H., Passano, E., Yttervik, R., Wu, J., Baarholm, G.S., 2017. VIVANA-Theory Manual, 4.10.1. SINTEF Ocean. Trondheim, Norway.

Lie, H., 2001. VIV Model Test of a Catenary Riser – STRIDE Ph. 4, Confidential report for 2H Offshore Engineering Ltd. Technical Report, Norwegian Marine Technology Research Institute, Trondheim, Norway.

Mo, K., 1999. Riser Model Test in Directionally Varying Current. Technical Report, Norwegian Marine Technology Research Institute, Trondheim, Norway.

Moe, G., Teigen, T., Simantiras, P., Willis, N., Lie, H., 2004. Predictions and model tests of an SCR undergoing VIV in flow at oblique angles. ASME Paper No. OMAE2004-51563.

Ogink, R.H.M., Metrikine, A.V., 2010. A wake oscillator with frequency dependent coupling for the modeling of vortex-induced vibration. J. Sound Vib. 329 (26), 5452–5473.

Riemer-Sørensen, S., Wu, J., Lie, H., Sævik, S., Kim, S.-W., 2019. Data-driven prediction of vortex-induced vibration response of marine risers subjected to three-dimensional current. In: Bach, K., Ruocco, M. (Eds.), Nordic Artificial Intelligence Research And Development. Springer International Publishing, Cham, pp. 78–89.

Sarpkaya, T., 2004. A critical review of the intrinsic nature of vortex-induced vibrations. J. Fluids Struct. 19 (4), 389–447.

Sarpkaya, T., Isaacson, M., 1981. Wave Forces On Offshore Structures. Van Nostrand Reinhold Company.

Schiller, R.V., Caire, M., Jaiswal, V., Nóbrega, P., E., P., H., L., Vortex induced vibrations of deep water risers: sensitivity to current profile, shear and directionality. ASME Paper No. OMAE2014-24141.

SINTEF Ocean, 2017. RIFLEX 4.10.0 Theory Manual. Trondheim, Norway.

Srinil, N., Zanganeh, H., 2012. Modelling of coupled cross-flow/in-line vortex-induced vibrations using double duffing and van der pol oscillators. Ocean Eng. 53, 83–97.

Swithenbank, S.B., 2007. Dynamics of Long Flexible Cylinders at High-Mode Number in Uniform and Sheared Flows (Ph.D. thesis). Massachusetts Institute of Technology, Cambridge, MA, USA.

Thorsen, M.J., Sævik, S., Larsen, C.M., 2014. A simplified method for time domain simulation of cross-flow vortex-induced vibrations. J. Fluids Struct. 49, 135–148.

Thorsen, M.J., Sævik, S., Larsen, C.M., 2016. Time domain simulation of vortex-induced vibrations in stationary and oscillating flows. J. Fluids Struct. 61, 1–19.
Thorsen, M.J., Sævik, S., Larsen, C.M., 2017. Non-linear time domain analysis of cross-flow vortex-induced vibrations. Mar. Struct. 51, 134–151.
Triantafyllou, M., Triantafyllou, G., Tein, Y.S.D., Ambrose, B.D., 1999. Pragmatic riser VIV analysis. In: Offshore Technology Conference, Paper NO. OTC-10931-MS.
Ulveseter, J.V., Thorsen, M.J., Sævik, S., Larsen, C.M., 2018. Time domain simulation of riser VIV in current and irregular waves. Mar. Struct. 60, 241–260.
Ulveseter, J.V., Thorsen, M.J., Sævik, S., Larsen, C.M., 2019. Simulating fundamental and higher harmonic VIV of slender structures. Appl. Ocean Res. 90.
Vandiver, J.K., Jaiswal, V., Jhingran, V., 2009. Insights on vortex-induced, traveling waves on long risers. J. Fluids Struct. 25 (4), 641–653.
Vandiver, J.K., Li, L., 2005. SHEAR7 V4.4 program theoretical manual. Department of Ocean Engineering, Massachusetts Institute of Technology. Cambridge, MA.
Vandiver, J.K., Swithenbank, S.B., Jaiswal, V., Jhingran, V., 2006. Fatigue damage from high mode number vortex-induced vibration. ASME Paper No. OMAE2006-92409.
Violette, R., de Langre, E., Szydlowski, J., 2007. Computation of vortex-induced vibrations of long structures using a wake oscillator model: Comparison with DNS and experiments. Comput. Struct. 85 (11), 1134–1141.
Voie, P.E., Larsen, C.M., Wu, J., Resvanis, T., 2016. VIV BEST PRACTICE: Guideline on Analysis of Vortex-Induced Vibrations in Risers and Umbilicals. Technical Report, Det Norske Veritas and Germanischer Lloyd, Oslo, Norway.
Wang, E., Xiao, Q., Incecik, A., 2017. Three-dimensional numerical simulation of two-degree-of-freedom VIV of a circular cylinder with varying natural frequency ratios at Re=500. J. Fluids Struct. 73, 162–182.
Williamson, C., Govardhan, R., 2008. A brief review of recent results in vortex-induced vibrations. J. Wind Eng. Ind. Aerodyn. 96 (6–7), 713–735.
Wu, J., Lie, H., Larsen, C.M., Liapis, S., Baarholm, R., 2016. Vortex-induced vibration of a flexible cylinder: Interaction of the in-line and cross-flow responses. J. Fluids Struct. 63, 238–258.